

# Building Interpretable Climate Emulators for Economics\*

Aryan Eftekhari<sup>†</sup> Doris Folini<sup>‡</sup> Aleksandra Friedl<sup>§</sup> Felix Kübler<sup>¶</sup>

Simon Scheidegger<sup>||</sup> Olaf Schenk<sup>\*\*</sup>

November 19, 2024

## Abstract

This paper presents a framework for developing efficient and interpretable carbon-cycle emulators (CCEs) as part of climate emulators in Integrated Assessment Models, enabling economists to custom-build CCEs accurately calibrated to advanced climate science. We propose a generalized multi-reservoir linear box-model CCE that preserves key physical quantities and can be use-case tailored for specific use cases. Three CCEs are presented for illustration: the 3SR model (replicating DICE-2016), the 4PR model (including the land biosphere), and the 4PR-X model (accounting for dynamic land-use changes like deforestation that impact the reservoir’s storage capacity). Evaluation of these models within the DICE framework shows that land-use changes in the 4PR-X model significantly impact atmospheric carbon and temperatures – emphasizing the importance of using tailored climate emulators. By providing a transparent and flexible tool for policy analysis, our framework allows economists to assess the economic impacts of climate policies more accurately.

**Keywords:** climate change, social cost of carbon, carbon taxes, environmental policy, deep learning, integrated assessment models, DICE-2016

**JEL classification:** C61, E27, Q5, Q51, Q54, Q58

---

\*We thank Christian Traeger as well as seminar participants at the University of Lausanne, the University of Zurich, as well as the EGU General Assembly Conference for very useful conversations and comments. The authors express their sincere gratitude to Pratyuksh Bansal for his contributions and dedication to spearheading the inception of this project. This work was supported by the Swiss National Science Foundation (SNSF), under project ID “Can Economic Policy Mitigate Climate-Change?”, and for research support.

<sup>†</sup>Institute of Computing, Università della Svizzera italiana; Email: [aryan.eftekhari@usi.ch](mailto:aryan.eftekhari@usi.ch).

<sup>‡</sup>Institute for Atmospheric and Climate Science, ETHZ; Email: [doris.folini@env.ethz.ch](mailto:doris.folini@env.ethz.ch).

<sup>§</sup>ifo Institute, Ludwig-Maximilian University of Munich; Email: [friedl@ifo.de](mailto:friedl@ifo.de).

<sup>¶</sup>Department for Banking and Finance, University of Zürich; Swiss Finance Institute (SFI); Email: [felix.kuebler@bf.uzh.ch](mailto:felix.kuebler@bf.uzh.ch).

<sup>||</sup>Department of Economics, University of Lausanne; Enterprise for Society (E4S); Email: [simon.scheidegger@unil.ch](mailto:simon.scheidegger@unil.ch)

<sup>\*\*</sup>Institute of Computing, Università della Svizzera italiana; Email: [olaf.schenk@usi.ch](mailto:olaf.schenk@usi.ch).

# 1 Introduction

**Motivation.** Integrated Assessment Models (IAMs) are essential tools in climate economics, providing a comprehensive framework to evaluate the interplay between economic systems and climate dynamics (Hassler, Krusell, and Olovsson, 2024). By capturing the nonlinear, dynamic, endogenous, and stochastic nature of economic and climate systems, IAMs are a fundamental pillar of informed decision-making and policy analysis (see, e.g., Fernández-Villaverde, Gillingham, and Scheidegger (2024) for a recent review). A key component of such IAMs is the *climate emulator* (CE), which provides a realistic quantitative link between anthropogenic carbon emissions and global warming at low computational costs.

Various climate emulators (CEs) exist, each designed to balance physical comprehensiveness with computational efficiency and interpretative transparency. Even relatively simple CEs, which reduce detail to improve computational cost and ease of interpretation, present challenges when adaptation and calibration are required to address specific, policy-relevant questions. Our focus here is on such simplified CEs, such as the widely used CE in the Dynamic Integrated Model of Climate and Economy (DICE) (Nordhaus, 2017), which employs a three-reservoir box-model<sup>1</sup> carbon-cycle emulator (CCE) alongside a two-reservoir temperature emulator. The latter is of no further concern here as it is largely fit for purpose in that global mean temperature is primarily governed by global oceans, whose surface and deep waters absorb 90% of the excess heat from climate change (Geoffroy et al., 2013a; von Schuckmann et al., 2023). In contrast, the three-reservoir CCE in DICE lacks the capacity to address policy-relevant questions that require, for instance, an explicit land carbon reservoir, such as those concerning land-use changes (e.g., deforestation) or specific carbon sequestration techniques. Modifying the rigid structure of the CCE poses significant challenges, particularly for users outside the CE community, even though such modifications would be desirable for quantitative modelers in economics.

**Contribution of the Paper.** We address this gap in the literature and the corresponding need among users by developing a comprehensive framework that enables modelers to construct any linear box-model type CCE required for their specific IAM and automatically calibrate it against climate datasets most appropriate for their analysis. Our computational framework employs constrained optimization techniques to fit custom-designed CCEs to benchmark data from Earth System Models (ESMs) or any other climate data sources chosen by the modeler. This flexibility ensures that the emulators are aligned with the most relevant and up-to-date climate science for their specific applications. To this end, we further offer a set of test cases to quantitatively evaluate the performance of a CCE under prescribed, policy-relevant scenarios. The focus on simple box-model CCEs is intentional, as they are transparent and interpretable by design. Our framework empowers economists and climate modelers to build interpretable and computationally efficient climate emulators tailored to their specific research questions and data preferences. As an illustration of our framework and to fill important gaps in the literature, we introduce three models: the **3SR model**, which replicates the DICE-2016 three-reservoir setup; the **4PR model**, which extends this by integrating the land biosphere as an explicit reservoir; and the **4PR-X model**, which further accommodates dynamic land-use changes, such as deforestation, that impact the carbon storage capacity of the reservoir. Evaluation of these CCEs within the DICE framework exemplifies the economic consequences of a dynamic land biosphere.

**Preview of Findings.** Our findings indicate several key points. *i)* In atmospheric perturbation experiments replicating calibration data from Joos et al. (2013) as well as controlled scenarios from Zickfeld et al. (2021) and MacDougall et al. (2020), both the 3SR and 4PR models show good performance on time scales up to 250 years. The models being linear by design, the choice of calibration determines whether atmospheric CO<sub>2</sub> concentrations tend to be slightly over- or under-estimated on time scales of several decades. *ii)* Using Representative Concentration Pathway (RCP) emissions

---

<sup>1</sup>A box model is a simplified representation of the Earth’s carbon cycle (and heat dynamics), dividing the system into interconnected reservoirs or “boxes” such as the atmosphere, ocean layers, and land. Each box exchanges carbon or heat with others, emulating key climate processes while balancing computational efficiency with interpretability. These models are widely used in IAMs to assess the climate impact of economic policies across various scenarios.

to model global CO<sub>2</sub> concentrations and average temperatures, we find that the improvements in the accuracy of the 4PR model over the 3SR model are not evident; both configurations yield very similar dynamics, underestimating temperatures and atmospheric carbon concentrations with increased emissions for the specific calibration chosen. Meanwhile, the 4PR-X model provides a better representation of CO<sub>2</sub> concentrations and average temperatures, particularly with increasing emissions. Our results indicate that even minor modifications to the equilibrium state (carbon storage capacity) of the land biosphere can markedly influence emission-driven simulations. *iii*) Finally, we evaluate the three carbon cycle models within the standard DICE economy-climate framework (Nordhaus, 2017). Our results show that while the 3SR and 4PR models yield similar simulation results relevant to policy-making, the 4PR-X model – which accounts for dynamic changes in the land biosphere due to deforestation or urbanization – delivers significantly higher atmospheric carbon masses and temperatures. This leads to stronger mitigation efforts and a higher social cost of carbon (SCC) in optimal policy scenarios. These findings imply that for accurate climate modeling and policy assessment, it is important to include the land biosphere reservoir to model land-use change. The presence of deforestation or urbanization affects optimal carbon policies non-trivially, underscoring the need for coordinated policies that address both industrial emissions and land management practices. In summary, our work establishes a robust and interpretable framework for modeling the carbon cycle in climate economics, specifically addressing limitations in existing models.

**Related literature.** Numerous CEs exist for use within IAMs, each designed to emulate the behavior of more complex ESMs with varying levels of detail while maintaining low computational cost. The simplest CEs compute global mean temperature change as a linear and instantaneous function of cumulative carbon emissions (Dietz and Venmans, 2019), with this linear relationship emerging as a non-trivial property in ESMs (MacDougall, 2016). Such models are valuable for their interpretability, despite the fact that the assumptions of instantaneous response and linearity only hold approximately (Raupach, 2013; Nicholls et al., 2020). However, without an explicit CCE, these models cannot explore the roles of distinct carbon reservoirs. Slightly more versatile is the CE in DICE, which features a three-reservoir box-model CCE and a two-reservoir temperature model. We argue that the box-model formulation of the CCE is more intuitive and adaptable for interpretation and use-case-specific modifications – including accommodation of non-linearities (Hooss et al., 2001; Zhang et al., 2021) – than the formally equivalent formulation using impulse response functions (IRFs) (Li, Jarvis, and Leedal, 2009; Raupach et al., 2011; Raupach, 2013). For this reason, we adopt the box-model formulation in this work, aiming to enable users to develop their own CCE that is interpretable, computationally efficient, and specifically tailored to their needs in terms of explicit carbon reservoirs.

More comprehensive CEs that extend beyond CO<sub>2</sub> and include other trace gases often utilize impulse response functions (IRFs) for the CCE, as in FAIR (Millar et al., 2017; Leach et al., 2021), OSCAR (Gasser et al., 2017), MCE (Tsutsui, 2022), HIRM (Dorheim, Smith, and Bond-Lamberty, 2021), and MAGICC (Meinshausen et al., 2011), rather than box models (as in DICE or Hector (Dorheim et al., 2024)), or a combination of both approaches (Bossy, Gasser, and Ciais, 2022; Sandstad et al., 2024). Some CEs also incorporate machine learning techniques (Watson-Parris et al., 2022) or provide spatially resolved outputs (Beusch, Gudmundsson, and Seneviratne, 2020; Quilcaille, Gudmundsson, and Seneviratne, 2023). Numerous CE comparison studies exist, focusing either solely on the climate components (Schwarber et al., 2019; Nicholls et al., 2021; Melnikova et al., 2023) or additionally addressing the economic consequences of the CE choice (Dietz et al., 2020). Our approach contributes to this literature by providing a framework to design a box-model CCE that is both interpretable and computationally efficient, specifically tailored to incorporate the land biosphere within IAMs like DICE.

To mitigate climate change, reducing current emissions is crucial, alongside implementing carbon dioxide removal (CDR) techniques to offset unavoidable emissions. Both strategies must be considered in economic studies that inform political decision-making. Several key CDR techniques rely on the management of land carbon reservoirs, such as forests and soils (Minx et al., 2018; Fuss et al., 2018; Nemet et al., 2018), which offer an estimated unrealized storage potential of several hundred petagrams

of carbon under present-day conditions (Walker et al., 2022; Mo et al., 2023), with the potential for even greater storage under future climate scenarios due to CO<sub>2</sub> fertilization (Ruehr et al., 2023). These estimates underscore the need to explicitly account for the land biosphere in cost-benefit models analyzing the economic aspects of climate change mitigation. However, to the best of our knowledge, only a few such cost-benefit studies currently exist.

Relatively few energy models incorporate forestry sequestration (Weyant, 2017), despite the emphasis on stabilization policies and the significant costs associated with meeting stringent concentration targets. While many existing models provide a detailed land-forest module, they often lack integration with ESMs. Studies analyzing the Agriculture, Forestry, and Other Land-Use (AFOLU) sector in models without an ESM component include Benítez et al. (2007), who present a framework for identifying least-cost afforestation and reforestation sites globally based solely on land-biosphere data without incorporating climate variables, and Hertel et al. (2008), who develop a framework to assess the mitigation potential of land-based emissions using GTAP data for land-forests. The critical role of ESMs in analyzing climate-related issues is emphasized in van Vuuren et al. (2012); Calvin et al. (2014).

Recently, there has been a surge in models that analyze land-forest components in conjunction with or fully integrated into the economy-climate block of IAMs. Studies utilizing sophisticated IAMs that make use of an emulator for the ESM include Calvin et al. (2014), who examine trade-offs between various bioenergy and land-use policies using GCAM, and Doelman et al. (2020), who assess the mitigation potential of afforestation with the IMAGE 3.0 model, confirming its substantial role in climate mitigation. While these models are highly detailed and comprehensive, most are classified as detailed-process models (Weyant, 2017; Krey et al., 2014). Unlike cost-benefit models, detailed-process models do not support welfare analysis. Additionally, their complexity often results in high computational costs, and their transparency can be challenging for policymakers.

There are specific instances of dynamic analysis, including cost-benefit analysis, applied to the AFOLU sector. For example, Sohngen et al. (2003, 2006) examine the potential role of forests in greenhouse gas mitigation under varying carbon prices, using the DICE model in conjunction with a global timber model (Sohngen, Mendelsohn, and Sedjo, 1999). However, a limitation of this approach is that DICE lacks an explicit land biosphere reservoir, which may influence the conclusions drawn from the forest analysis.

**Organization of Paper.** The remainder of the paper is organized as follows: Section 2 outlines the class of CCEs we consider. Section 3 discusses the generic optimization strategy we propose for calibrating these CCEs for use within a complete CE. Section 4 presents three types of numerical experiments that illustrate how our methodology can be used to construct custom-made CCEs and fit them to chosen benchmark data. Section 5 then explores the implications of these choices in dynamic economic applications. Finally, Section 6 concludes. The related code framework is available at [https://github.com/ClimateChangeEcon/Building\\_Interpretable\\_Climate\\_Emulators\\_forEconomics](https://github.com/ClimateChangeEcon/Building_Interpretable_Climate_Emulators_forEconomics).

## 2 Carbon Cycle

In this section, we present the most general structure of the linear box models for the carbon cycle considered in this article. The carbon cycle governs atmospheric carbon concentrations, influencing global temperatures through interactions among multiple carbon reservoirs. Our aim is to illustrate to quantitative economists how transparent CCEs can be selected to optimally address specific research questions within a given IAM. To this end, we discuss three concrete cases of CCEs.

We begin in Section 2.1 with a formal description of a multi-reservoir linear carbon cycle involving three reservoir classes: atmosphere (A), ocean (O), and land biosphere (L). We examine a three-reservoir model in a “serial” configuration (3SR), where the carbon cycle is modeled with three sequentially connected reservoirs: the atmosphere, followed by two ocean reservoirs. We also introduce a novel four-reservoir model in a “parallel” configuration (4PR), where atmospheric carbon is divided

into parallel flows toward the land biosphere and oceans (see Figure 1). In Section 2.2, we expand the 4PR configuration by introducing a dynamic variant (4PR-X), which uses a time-dependent operator to capture changes in the equilibrium state of the carbon cycle. This allows us to simulate scenarios with reduced carbon absorption capacity, such as those affected by deforestation. In Section 2.3, we address challenges in the parameter-fitting procedure for these models, underscoring the need for the methodology presented in Section 3. These models are then all used in a set of simulations, which are described in detail in Section 4.

## 2.1 Multi-Reservoir Model

Let  $\mathbf{m}^t \in \mathbb{R}^n$  represent the carbon masses of  $n$  reservoirs at discrete time steps  $t = 0, 1, \dots, T - 1$ . The carbon cycle model is defined by an operator  $\mathbf{A} \in \mathbb{R}^{n \times n}$ , which determines the rates of carbon mass exchange between reservoirs (in the simplest case, we assume a time-invariant operator; see Section 2.2 for details on the time-dependent operator), as illustrated in Figure 1.

With emissions<sup>2</sup> denoted as  $\mathbf{e}^t \in \mathbb{R}^n$ , we describe the carbon cycle using a first-order system of difference equations:

$$\mathbf{m}^{t+1} - \mathbf{m}^t = \mathbf{A}\mathbf{m}^t + \mathbf{e}^t, \quad (1)$$

where  $\mathbf{m}^0$  is the *initial condition*, which is assumed to be known. Unless stated otherwise, we assume an implicit unit time step throughout.

The operator  $\mathbf{A}$  has real eigenvalues satisfying  $-1 < \lambda_i(\mathbf{A}) \leq 0$  for all  $i$ . For each pair of reservoirs  $i$  and  $j$ , a carbon transfer pathway exists if  $\mathbf{A}_{ij} \neq 0$ , and no pathway exists if  $\mathbf{A}_{ij} = 0$ .

Additionally,  $\mathbf{A}$  is constrained by both an *equilibrium condition* and *mass conservation*. The equilibrium condition is defined by:

$$\mathbf{A}\tilde{\mathbf{m}} = \mathbf{0}, \quad (2)$$

where  $\tilde{\mathbf{m}}$  represents the equilibrium carbon masses, proportional to the eigenvector associated with the zero eigenvalues of  $\mathbf{A}$ .

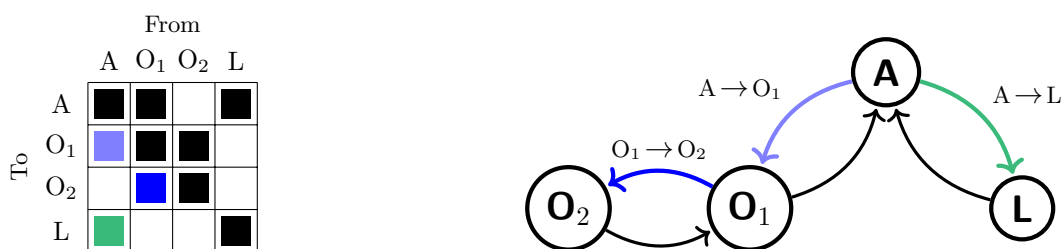


**Figure 1:** The operator  $\mathbf{A}$  is visualized for the 4PR model (left), which includes the atmosphere (A), upper ocean ( $O_1$ ), lower ocean ( $O_2$ ), and land biosphere (L) reservoirs. The connectivity of the reservoirs is shown (right) with unknown carbon mass transfer rates, where, for example,  $O_1 \rightarrow O_2$  corresponds to the entry  $\mathbf{A}_{3,2}$ . The nonzero pattern of  $\mathbf{A}$  is symmetric, but the values are not. Setting  $\mathbf{A}_{4,1} = 0$  yields the 3SR model; see Appendix A for more details.

<sup>2</sup>Emissions can originate from both anthropogenic sources and natural processes.

The principle of mass conservation<sup>3</sup> is upheld by ensuring that for all  $t$  the following holds:

$$\mathbf{1}^\top(\mathbf{m}^{t+1} - \mathbf{m}^t) = \mathbf{1}^\top \mathbf{e}^t \iff \mathbf{1}^\top \mathbf{A} = \mathbf{0}. \quad (3)$$

We define the *dynamic timescales* of the operator as  $\tau_i = 1/|\lambda_i|$ . Consequently, the possible dynamic timescales for the linear carbon cycle model are  $\tau_i \in (1, \infty)$ . The zero eigenvalue and the associated infinite dynamic timescale correspond to the equilibrium condition. For reporting purposes, we will exclude the zero eigenvalue and its corresponding dynamic timescale.

Next, we denote  $\mathcal{I} := \{(i, j) : \mathbf{A}_{ij} \neq 0, i > j\}$  as the strictly lower triangular nonzero indices of  $\mathbf{A}$ . For all model configurations, the upper triangular values of the operator satisfying both (2) and (3) are given by:

$$\mathbf{A}_{ji} = \mathbf{A}_{ij} \cdot \frac{\tilde{\mathbf{m}}_j}{\tilde{\mathbf{m}}_i} \quad \forall (i, j) \in \mathcal{I}, \text{ and } \mathbf{A}_{ii} = - \sum_{j=1, j \neq i}^p \mathbf{A}_{ji}. \quad (4)$$

The parameters defining the operator, denoted  $\mathbf{A}[\mathbf{a}, \tilde{\mathbf{m}}]$ , are the strictly lower triangular nonzero elements  $\mathbf{a} := \{\mathbf{A}_{ij} : (i, j) \in \mathcal{I}\}$ , along with the equilibrium masses  $\tilde{\mathbf{m}}$ . The set of *admissible parameters* includes those that satisfy  $-1 < \lambda_i(\mathbf{A}[\mathbf{a}, \tilde{\mathbf{m}}]) \leq 0$ . For a predefined sequence of emissions  $\mathbf{E} := (\mathbf{e}^1, \mathbf{e}^2, \dots, \mathbf{e}^T)$  of length  $T$ , the resulting carbon cycle simulation is denoted as

$$\mathbf{M}[\mathbf{a}, \tilde{\mathbf{m}}] := (\mathbf{m}^1, \mathbf{m}^2, \dots, \mathbf{m}^T), \quad (5)$$

where each  $\mathbf{m}^t$  is defined according to (1). In what follows, we use the acronyms shown in Figure 1 to refer to specific reservoirs; for example,  $\mathbf{M}[\mathbf{a}, \tilde{\mathbf{m}}]_{\text{O}_2}^t$  (or simply  $\mathbf{m}_{\text{O}_2}^t$  when  $\mathbf{a}$  and  $\tilde{\mathbf{m}}$  need not be emphasized) represents the content of the O<sub>2</sub> (deep ocean) reservoir at time  $t$ .

Although this is a simple linear model, it establishes a fundamental baseline for characterizing the complex nonlinear dynamics of more sophisticated carbon cycle models. For example, consider  $f : \mathbf{m}^t \rightarrow (\mathbf{m}^{t+1} - \mathbf{m}^t)$  as a smooth function that captures the full scope of carbon cycle dynamics, adhering to both a stable equilibrium state  $f(\tilde{\mathbf{m}}^t) = \mathbf{0}$  and mass conservation  $\mathbf{1}^\top f(\mathbf{m}^t) = 0$ .

The first-order approximation of  $f$  around a given state  $\bar{\mathbf{m}}$  is given by:

$$f(\mathbf{m}^t) \approx f(\bar{\mathbf{m}}) + \partial f(\bar{\mathbf{m}})(\mathbf{m}^t - \bar{\mathbf{m}}), \quad (6)$$

where  $\partial f(\bar{\mathbf{m}}) \in \mathbb{R}^{n \times n}$  denotes the Jacobian matrix. If this approximation is performed at  $\bar{\mathbf{m}} = \tilde{\mathbf{m}}$ , letting  $\mathbf{A} := \partial f(\tilde{\mathbf{m}})$ , the expression in (6) reduces to (1) when emissions are excluded. Starting from pre-industrial conditions, this approximation of  $f$  has an error of  $\mathcal{O}(\|\mathbf{m}^t - \tilde{\mathbf{m}}\|^2)$ .

## 2.2 Time-Dependent Operator

The operator  $\mathbf{A}$ , as defined in (4), is constant, assuming a fixed equilibrium partitioning of total carbon mass across the various reservoirs (ratios  $\tilde{\mathbf{m}}_j/\tilde{\mathbf{m}}_i$ ) and constant exchange coefficients between reservoirs (coefficients  $\mathbf{A}_{ij}$ ). As discussed in Hurtt et al. (2011) and Meinshausen et al. (2011), land-use-related emissions (see also Figure 7) are primarily driven by activities such as permanent deforestation and agricultural expansion, which alter the storage capacity of the land biosphere. Consequently, the equilibrium carbon mass in the land reservoir is no longer constant within the box model framework.

---

<sup>3</sup>The principle of mass conservation states that the total mass in a closed system remains constant over time, meaning that mass can only be re-distributed, but is neither created nor destroyed. In the context of the carbon cycle, this principle ensures that the total carbon mass across all reservoirs remains constant, regardless of internal exchanges among reservoirs.

In what follows, we propose a *time-dependent* operator, which utilizes the baseline 4PR model configuration while also accounting for changes in the equilibrium masses of the land biosphere  $\tilde{\mathbf{m}}_L$ . Given land-use change emissions  $\mathbf{e}_L^t$  at time  $t$ , and assuming that a fraction  $r$  of these emissions is due to deforestation, the equilibrium mass of the land biosphere at the next time step is given by:

$$\tilde{\mathbf{m}}_L^{t+1} = \tilde{\mathbf{m}}_L^t - r \cdot \mathbf{e}_L^t, \quad (7)$$

which results in a time-dependent version of the operator in (4). For our simplified model, we assume a one-to-one ( $r = 1$ ) relationship between each unit of land-use emission and a corresponding reduction in  $\tilde{\mathbf{m}}_L$ , so that all emissions from land-use change directly reduce the equilibrium mass of the land-biosphere reservoir. Notably, the equilibrium mass of the land biosphere in the box model only approximates the actual carbon stored in the land biosphere.<sup>4</sup> One may go beyond this simplified approach by introducing a proportionality constant for adjusting the relationship between land-use change emissions and the equilibrium mass in the land-biosphere reservoir box.<sup>5</sup>

The rate of change with respect to  $\tilde{\mathbf{m}}_L^t$  (see Appendix A for details on the carbon reservoir mass equations) for the atmospheric and land biosphere reservoirs is given by

$$\frac{\partial \mathbf{m}_A^{t+1}}{\partial \tilde{\mathbf{m}}_L^t} \propto \frac{-1}{(\tilde{\mathbf{m}}_L^t)^2}, \text{ and } \frac{\partial \mathbf{m}_L^{t+1}}{\partial \tilde{\mathbf{m}}_L^t} \propto \frac{1}{(\tilde{\mathbf{m}}_L^t)^2}. \quad (8)$$

Consequently, we expect that reducing the equilibrium mass of the land biosphere will lead to a decrease in the amount of carbon transferred (i) out of the atmosphere and (ii) into the land biosphere. For further details, see the simulation results in Section 4.2.

### 2.3 Challenges of Degrees of Freedom

A major challenge for a climate emulator is selecting parameters that enable the simplified model to accurately reflect the carbon cycle dynamics of more complex models. A common approach to fitting parameters involves solving an optimization problem that minimizes the error between the emulator’s simulation and benchmark results. However, this often results in an ill-posed optimization problem, where parameters may take on a range of values that, while yielding similar carbon flux responses, do not align with real-world observations.

This issue arises in part from (4), where only the ratios of the equilibrium masses are essential in defining  $\mathbf{A}$ . Consequently, for any scalar  $c$ , the parameters  $c \cdot \tilde{\mathbf{m}}$  produce equivalent results. In Section 3, we introduce a fitting procedure that addresses these challenges by incorporating physics-informed constraints and leveraging the model’s linearity to construct a weighted operator, capturing extreme dynamics across different model configurations.

## 3 Climate Emulator

In this section, we illustrate how a box-type CCE, selected according to a modeler’s specific needs, can be systematically fitted to state-of-the-art data. We further demonstrate how the fitted CCE can be merged with a temperature module to create a complete climate emulator. Note that throughout, we consider an emulator to consist of both the carbon cycle model and the temperature model.

In Section 3.1, we outline our proposed generic fitting procedure, including parameter selection and hyperparameter calibration for the linear model. To illustrate our procedure, we take advantage

<sup>4</sup>This is in contrast to atmospheric carbon, for which the absolute quantities in the model and in reality align, with 589 GtC in 1750 (see Table 1).

<sup>5</sup>For example, if the model’s land reservoir is half the size of the real land-biosphere carbon content (250 GtC instead of 500 GtC), an emission of 1 GtC per year from land-use change could be modeled by emitting the full 1 GtC to the atmosphere box, while reducing the equilibrium mass of the model land-biosphere by only 0.5 GtC.

of Joos et al. (2013), who offer a database of the simulated decay of an instantaneous carbon pulse. Individual simulations differ, among others, in the climate model used, the amplitude of the pulse, or the background conditions into which the pulse is released. Here, we use the multi-model mean (average over more than ten individual models) of the simulated decay of a 100 GtC carbon pulse under pre-industrial (PI) conditions, corresponding to the year 1750. Appendix C provides a corresponding illustration of our method for present-day (PD) background conditions, representative of the year 2010. We stress that any other carbon pulse decay data, from Joos et al. (2013) or any other data source, may be used to calibrate the CCE. The choice is to be guided by the envisaged use-case, for example, whether one is interested in an average or an extreme pulse decay (see also Folini et al. (2024)) or what background conditions (PI, PD, other) seem most appropriate.

Next, in Section 3.2, we outline the temperature model and its parameterization, which is primarily based on the work of Geoffroy et al. (2013a,b), with slight adjustments to account for external radiative forcing factors.

### 3.1 Carbon Cycle Fitting Procedure

The proposed parameter fitting procedure captures pulse decay dynamics through a two-step process outlined in Sections 3.1.1 and 3.1.2. First, we optimize model parameters to emulate the mean atmospheric pulse decay trajectory based on a set of simulation benchmarks. Second, we introduce a scaling approach to adjust the fitted model for capturing extreme carbon cycle responses.

The simulation benchmarks represent atmospheric CO<sub>2</sub> decay trajectories following a 100 GtC pulse in various models with the carbon cycle at equilibrium.<sup>6</sup> As an example of benchmark data used below, Figure 2 shows the multimodel mean, denoted as  $\mu$ , with  $\mu^+$  and  $\mu^-$  representing two standard deviations above and below  $\mu$ , respectively.

#### 3.1.1 Mean Parameters

Let  $\mathbf{y}^\mu \in \mathbb{R}^T$  denote the atmospheric decay trajectory for the  $\mu$ -benchmark for  $T$  years after the introduction of the 100 GtC pulse. The *fit error*, which is measured solely based on the deviation

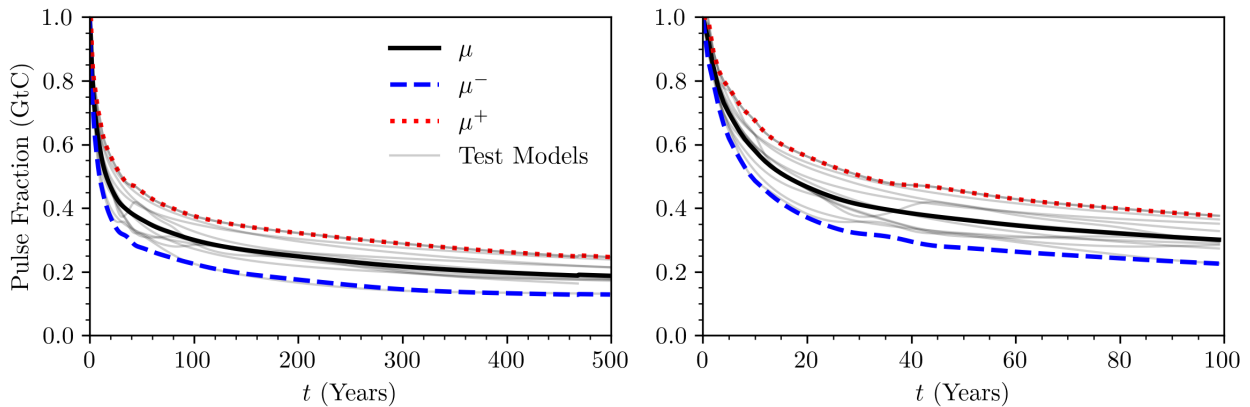


**Figure 2:** Simulations by Joos et al. (2013) illustrate the decay of a 100 GtC pulse over the first 500 years (left) and 100 years (right) under pre-industrial (PI) conditions, corresponding to the year 1765 with the Earth’s carbon cycle at equilibrium. The simulated pulse decay across various test models, including ESMs, ESMIC, and four box-type models, is shown alongside the multimodel mean ( $\mu$ ), with  $\mu^+$  and  $\mu^-$  representing two standard deviations above and below  $\mu$ , respectively.

<sup>6</sup>See [https://climatehomes.unibe.ch/~joos/IRF\\_Intercomparison/results.html](https://climatehomes.unibe.ch/~joos/IRF_Intercomparison/results.html) for further details.

between the emulated atmospheric masses and the  $\mu$ -benchmark, is defined as<sup>7</sup>

$$\mathcal{L}(\mathbf{a}^\mu, \tilde{\mathbf{m}}^\mu) := \frac{1}{T} \left\| \mathbf{M}[\mathbf{a}, \tilde{\mathbf{m}}]_{\text{A}} - \mathbf{y}^\mu \right\|_2. \quad (9)$$

The masses of non-atmospheric reservoirs are indirectly controlled through a penalty function which imposes penalties on solutions that do not align with observed carbon cycle attributes. These attributes are encoded through penalty functions  $q_1$ ,  $q_2$ , and  $q_3$ , which are related to (i) dynamic timescales, (ii) variability in equilibrium masses, and (iii) reservoir absorption ratios, respectively.<sup>8</sup> Given the non-negative scalar hyperparameters  $\rho_1$ ,  $\rho_2$ , and  $\rho_3$ , each corresponding to the respective penalty functions, the  $\mu$ -benchmark fitted parameters are

$$\left\{ \mathbf{a}^\mu, \tilde{\mathbf{m}}^\mu \right\} = \underset{\{\mathbf{a}, \tilde{\mathbf{m}}\}}{\operatorname{argmin}} \left\{ \mathcal{L}(\mathbf{a}^\mu, \tilde{\mathbf{m}}^\mu) + \rho_1 q_1(\mathbf{a}, \tilde{\mathbf{m}}) + \rho_2 q_2(\tilde{\mathbf{m}}) + \rho_3 q_3(\mathbf{a}, \tilde{\mathbf{m}}) \right\}. \quad (10)$$

In our tests, we use  $T = 250$  aligning with the time scales associated with the carbon exchange between the atmosphere and the Earth's surface, ranging from decades to centuries.

**Dynamic Timescales ( $q_1$ ):** In addition to accounting for carbon exchange between the atmosphere and the Earth's surface, we also consider the long-term carbon cycles of the deep ocean, which operate over time frames ranging from centuries to millennia (see, e.g., [Ciais et al. \(2014\)](#), and references therein).

To better capture these extended carbon cycle processes—particularly those with longer dynamic timescales, we include the penalty function:

$$q_1(\mathbf{a}, \tilde{\mathbf{m}}) := -\frac{1}{n} \operatorname{tr}(\mathbf{A}[\mathbf{a}, \tilde{\mathbf{m}}]) = -\frac{1}{n} \sum_{i=1}^n \lambda_i(\mathbf{A}[\mathbf{a}, \tilde{\mathbf{m}}]). \quad (11)$$

This adjustment biases the optimization program toward operators  $\mathbf{A}[\mathbf{a}, \tilde{\mathbf{m}}]$  with smaller average eigenvalues or, equivalently, larger average timescales.

**Equilibrium Mass Variability ( $q_2$ ):** The optimization problem in (10) is non-convex, as evident in (4), where only the ratios of  $\tilde{\mathbf{m}}$  are relevant, making scalar multiples of  $\tilde{\mathbf{m}}$  equivalent. Consequently, we can expect significant variability in the fitted parameters  $\mathbf{a}$  and  $\tilde{\mathbf{m}}$ .

To address this issue, we introduce a bias in the objective to align  $\tilde{\mathbf{m}}$  with existing estimates of PI carbon reservoir masses. Let  $\tilde{\mathbf{m}}^*$  denote these estimated equilibrium masses of the reservoirs. We penalize the relative difference between  $\tilde{\mathbf{m}}$  and  $\tilde{\mathbf{m}}^*$  using the penalty function

$$q_2(\tilde{\mathbf{m}}) := \frac{1}{n} \left\| (\tilde{\mathbf{m}} - \tilde{\mathbf{m}}^*) \oslash \tilde{\mathbf{m}}^* \right\|_2, \quad (12)$$

where  $\oslash$  denotes element-wise division. In our tests,  $\tilde{\mathbf{m}}^*$  is defined based on the pre-industrial (PI) estimates from [Ciais et al. \(2014\)](#), where the equilibrium masses of the reservoirs for the atmosphere, upper ocean, lower ocean, and land biosphere are 589, 900, 37100, and 550 GtC, respectively.

We emphasize that the values of  $\tilde{\mathbf{m}}^*$  do not represent the absolute total equilibrium masses of carbon in each reservoir. Instead, they estimate the carbon masses actively involved in the carbon

<sup>7</sup>Note that [Folini et al. \(2024\)](#) used the maximum norm, whereas we take the 2-norm. The maximum norm was chosen to have a decent fit early on in the pulse decay, while the 2-norm gives more weight to the long-term evolution of the decay. The long-term evolution refers to the length of the fitting period, 250 years here, whereas it is 100 years in [Folini et al. \(2024\)](#). We stress that either choice is viable.

<sup>8</sup>The number of penalty functions can be increased arbitrarily to match, for instance, additional physical properties of the carbon cycle. However, special care should be taken to avoid redundancy.

cycle dynamics of the atmosphere, oceans, and land biosphere. In contrast, carbon masses in fossil fuel reserves, permafrost, and dead organic matter in litter and soils are excluded from these equilibrium masses.<sup>9</sup>

**Reservoir Absorption Ratios ( $q_3$ ):** Cumulative carbon fluxes from the atmosphere to the ocean and land biosphere reservoirs significantly shape the emulator’s overall response characteristics. For instance, in the context of a 100 GtC pulse, the 4PR configuration could plausibly achieve a good fit for the atmospheric decay trajectory while maintaining minimal cumulative flux to the land biosphere reservoir—effectively mimicking the behavior of the 3SR model, which lacks a land biosphere reservoir (see Section 2.1 for further details).

To ensure the model reflects the observed dynamics of more complex ESMs, we enforce the ratio of cumulative ocean and land biosphere fluxes from the onset of pulse emissions. Let  $\eta$  represent the ratio of the cumulative ocean to land biosphere fluxes at time  $t_e$ ; deviations from this target are penalized by

$$q_3(\mathbf{a}, \tilde{\mathbf{m}}) := \left\| \frac{\mathbf{M}[\mathbf{a}, \tilde{\mathbf{m}}]_{\text{O}}^{t_e}}{\mathbf{M}[\mathbf{a}, \tilde{\mathbf{m}}]_{\text{L}}^{t_e}} - \eta \right\|_2, \quad (13)$$

where  $\mathbf{M}[\mathbf{a}, \tilde{\mathbf{m}}]_{\text{O}}^{t_e}$  is the total mass of all ocean reservoirs, and  $\mathbf{M}[\mathbf{a}, \tilde{\mathbf{m}}]_{\text{L}}^{t_e}$  denotes the total mass of all land biosphere reservoirs.

Following the findings of Joos et al. (2013), we set  $\eta = 1$ , corresponding to equal distribution of 30 GtC between ocean and land biosphere reservoirs at  $t_e = 20$  years after a 100 GtC atmospheric pulse.

### 3.1.2 Extrema Parameters

As shown in Figure 2, various ESMs exhibit different rates of 100 GtC pulse decay trajectories. Here, we aim to capture the extrema—defined as two standard deviations above and below the mean—of these trajectories across different ESMs. Like the mean fitting procedure described above, these dynamics are not tied to any specific ESM. Rather, they represent plausible upper and lower limits for atmospheric carbon content during a pulse event. Here, we assume that these plausible upper and lower limits are two standard deviations above and below the  $\mu$ -benchmark, denoted as the  $\mu^+$  and  $\mu^-$ -benchmark, respectively. Given the pulse decay trajectories  $\mathbf{y}^{\mu^+}, \mathbf{y}^{\mu^-} \in \mathbb{R}^T$ , we define

$$c^{\mu^+} = \underset{c}{\operatorname{argmin}} \left\{ \frac{1}{T} \left\| \mathbf{M}[c \cdot \mathbf{a}^{\mu}, \tilde{\mathbf{m}}^{\mu}]_{\text{A}} - \mathbf{y}^{\mu^+} \right\|_2 \right\}, \text{ and } c^{\mu^-} = \underset{c}{\operatorname{argmin}} \left\{ \frac{1}{T} \left\| \mathbf{M}[c \cdot \mathbf{a}^{\mu}, \tilde{\mathbf{m}}^{\mu}]_{\text{A}} - \mathbf{y}^{\mu^-} \right\|_2 \right\}, \quad (14)$$

as positive coefficients corresponding to the  $\mu^+$  and  $\mu^-$  benchmarks, respectively. For  $\mathbf{A}^{\mu} := \mathbf{A}[\mathbf{a}^{\mu}, \tilde{\mathbf{m}}^{\mu}]$ , we define the respective extrema operators as  $\mathbf{A}^{\mu^+} := c^{\mu^+} \cdot \mathbf{A}^{\mu}$  and  $\mathbf{A}^{\mu^-} := c^{\mu^-} \cdot \mathbf{A}^{\mu}$ . In our test, we keep  $T$  consistent with the value used in (10).

Note that  $\mathbf{A}^{\mu^+}$  and  $\mathbf{A}^{\mu^-}$  are scaled versions of  $\mathbf{A}^{\mu}$ , with all eigenvalues multiplied by  $c^{\mu^+}$  and  $c^{\mu^-}$ , respectively.<sup>10</sup> Adjusting the eigenvalues also shifts the range of dynamic timescales. The solution of (14) will satisfy  $c^{\mu^+} < 1 < c^{\mu^-}$ . Due to the linearity of the carbon cycle model, we can formulate a parameterized weighted operator that inherently satisfies the conditions outlined in Section 2.1, including the equilibrium condition and mass conservation. Given  $\alpha \in [-1, 1]$ , the weighted operator is defined as

<sup>9</sup>Carbon in fossil fuel reserves, permafrost, and dead organic matter in litter and soils becomes relevant only over much longer timescales, ranging from multiple centuries to millennia.

<sup>10</sup>Specifically,  $\mathbf{A}[c \cdot \mathbf{a}, \tilde{\mathbf{m}}]$  is equivalent to  $c \cdot \mathbf{A}_{ij}$ ; see (4) for details.

$$\mathbf{A}^\alpha := \begin{cases} (1 - \alpha)\mathbf{A}^\mu + \alpha\mathbf{A}^{\mu^+} & \text{if } \alpha > 0, \\ (1 + \alpha)\mathbf{A}^\mu - \alpha\mathbf{A}^{\mu^-} & \text{if } \alpha \leq 0, \end{cases} \quad (15)$$

where  $\alpha = 0$  represents the mean atmospheric carbon content across various ESMs. Setting  $\alpha = 1$  or  $\alpha = -1$  emulates ESMs with higher or lower atmospheric carbon content, respectively, corresponding to slower or faster carbon absorption from the atmosphere. It is important to note that weighting the operator scales the carbon transfer rates to align atmospheric carbon concentrations with the specified maximum or minimum benchmark values. Relative to the unweighted operator ( $\alpha = 0$ ), the weighted operator can adjust the dynamic timescales ( $q_1$ ) and reservoir absorption ratios ( $q_3$ ), while the equilibrium mass variable ( $q_2$ ) remains unchanged, as  $\mathbf{A}^\alpha \mathbf{m}^\mu = \mathbf{0}$  for all values of  $\alpha$ . This approach to extreme CCE calibrations enables assessment of the relevance of these extremes to the intended use case. If the answer is affirmative – that extreme calibrations of the CCE are potentially relevant for the (economic) question under consideration—we caution that simple operator scaling may be insufficient. In such cases, the CCE should instead be re-calibrated to specifically selected extreme scenarios, as discussed in [Folini et al. \(2024\)](#).

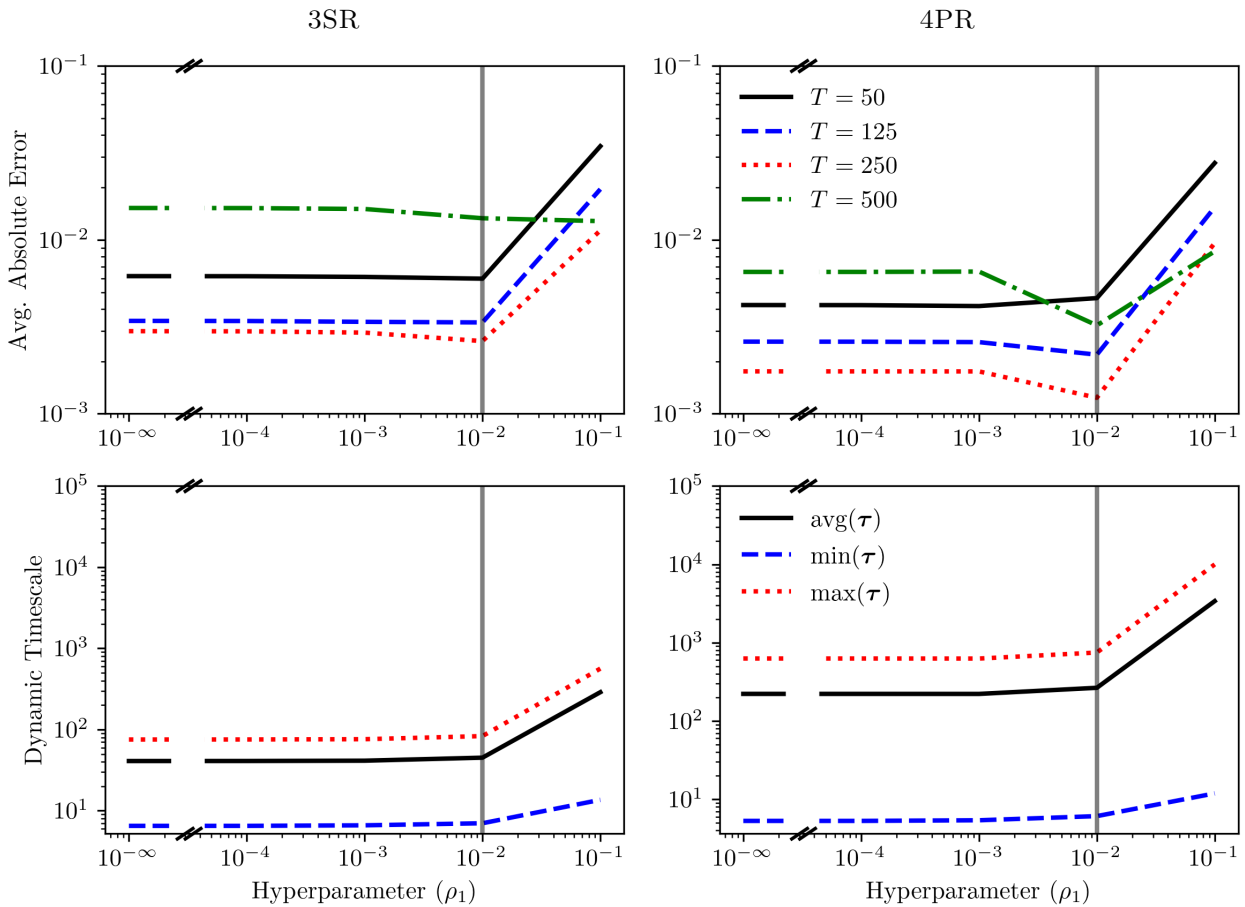


**Figure 3:** Average absolute error ( $\|\mathbf{m}_A - \mathbf{y}^\mu\|_1/T$ ) and dynamic timescales  $\tau$  for the 3SR (left column) and 4PR (right column) model configurations, shown across varying values of  $\rho_1$  with fixed values  $\rho_2 = \rho_3 = 10^{-4}$ . The average absolute error represents the mean absolute difference between the emulator simulation and the  $\mu$ -benchmark over a time span of  $T$  years following a 100 GtC carbon pulse. The vertical line indicates the selected value of  $\rho_1 = 10^{-2}$ .

### 3.1.3 Calibrating Hyperparameters

In what follows, we discuss the selection of hyperparameters. We first focus on  $\rho_2$  and  $\rho_3$ , which relate to equilibrium mass variability and reservoir absorption ratios, respectively (cf. Section 3.1.1).

Generally, smaller values for these hyperparameters are preferred to prevent the penalty functions from overpowering the model fit error (9). Our numerical results for the 4PR model configuration indicate that setting  $\rho_2 = \rho_3 = 10^{-4}$  minimizes the fit error while achieving desirable low equilibrium mass variations and reservoir absorption ratios. The results are similar for the 3SR configuration, except that  $q_3$  has no effect on the model due to the absence of a land biosphere. Therefore, we set  $\rho_3 = 0$ .

To justify the selection of  $\rho_1$ , we analyze the fit error relative to the  $\mu$ -benchmark over a simulation time period ranging from  $T = 50$  to  $T = 500$ . As parameter fitting is performed for  $T = 250$ , our analysis will cover both in-sample and out-of-sample error. In Figure 4, we show the average absolute error of atmospheric carbon content relative to the  $\mu$ -benchmark and the dynamic timescales  $\tau$  across varying values of  $\rho_1$ .

The 3SR model exhibits minimal sensitivity to  $\rho_1$ , which supports extended dynamic timescales. However, in the 4PR model, we observe reductions in the average absolute error as  $\rho_1$  increases.

As expected, increasing  $\rho_1$  results in larger dynamic timescales in both model configurations. The 3SR model can represent only two dynamic timescales, corresponding to its two nonzero eigenvalues, while the 4PR model can represent three. We observe that while the 3SR model can capture short-term dynamics, it lacks the versatility to accurately represent short, medium, and long-term timescales simultaneously, tending instead to average out medium and long-term behaviors.

We select  $\rho_1 = 10^{-2}$  for both the 3SR and 4PR configurations.

For a detailed analysis of hyperparameter calibration, see Appendix B. For the 3SR model configuration, we use hyperparameters  $\rho_1 = 10^{-2}$ ,  $\rho_2 = 10^{-4}$ , and  $\rho_3 = 0.0$ . For the 4PR configuration, we set  $\rho_1 = 10^{-2}$ ,  $\rho_2 = 10^{-4}$ , and  $\rho_3 = 10^{-4}$ . Using these hyperparameters, the model parameters for both configurations are presented in Table 1. With these settings, the extrema parameters  $c^{\mu+}$  and  $c^{\mu-}$  are fitted according to (14). These values are approximately the same for both the 3SR and 4PR configurations. The mass transfer rates  $\mathbf{a}^\mu$  are notably larger in the 3SR configuration compared to the 4PR configuration. In contrast, the equilibrium masses  $\tilde{\mathbf{m}}^\mu$  in the 4PR configuration are significantly larger than those in the 3SR configuration and closely align with the equilibrium masses reported in Ciais et al. (2014) (see discussion related to (12)).

## 3.2 Temperature Model

The temperature change is governed by a time-dependent radiative forcing amplitude parameter ( $\mathcal{F}^t$ ) at discrete time  $t$ , along with the following set of free parameters: the combined heat capacity of the atmosphere, land biosphere, and upper ocean ( $C$ ); the deep-ocean heat capacity ( $C_0$ ); the heat exchange coefficient ( $\gamma$ ); and the radiative feedback parameter ( $\lambda$ ). Let  $\mathbf{x}^t \in \mathbb{R}^2$  represent the global temperature at time  $t$  in a two-layered system, where  $\mathbf{x}_1^t$  denotes the temperature of the atmosphere, land biosphere, and upper ocean, and  $\mathbf{x}_2^t$  represents the temperature of the deep ocean. The temperature dynamics are modeled as a first-order system of difference equations, expressed as

$$\mathbf{x}^{t+1} - \mathbf{x}^t = \Delta t \cdot (\mathbf{A}\mathbf{x}^t + \mathbf{b}^t), \text{ where } \mathbf{A} := \begin{bmatrix} -(\lambda + \gamma)/C & \gamma/C \\ \gamma/C_0 & -\gamma/C_0 \end{bmatrix}, \text{ and } \mathbf{b}^t := \begin{bmatrix} \mathcal{F}^t/C \\ 0 \end{bmatrix}. \quad (16)$$

The summary statistics are presented in Table 2. The total radiative forcing is modeled as a function of the relative CO<sub>2</sub> concentration, following the formulation of Houghton, Jenkins, and Ephraums (1990). To account for additional factors, we scale the CO<sub>2</sub> relative forcing by a factor of  $\kappa$ , giving

$$\mathcal{F}^t := \kappa \cdot \frac{\mathcal{F}_{2 \times \text{CO}_2}}{\ln(2)} \cdot \ln \left( \frac{\mathbf{m}_A^t}{\mathbf{m}_A^0} \right), \quad (17)$$

	FITTED PARAMETERS VALUES										
	$\mathbf{a}_{A \rightarrow O_1}^\mu$	$\mathbf{a}_{O_1 \rightarrow O_2}^\mu$	$\mathbf{a}_{A \rightarrow L}^\mu$	$\tilde{\mathbf{m}}_A^\mu$	$\tilde{\mathbf{m}}_{O_1}^\mu$	$\tilde{\mathbf{m}}_{O_2}^\mu$	$\tilde{\mathbf{m}}_L^\mu$	$\mathbf{c}^{\mu^+}$	$\mathbf{c}^{\mu^-}$	$\mathbf{m}_O^{t_e}/\mathbf{m}_L^{t_e}$	$\tau$
<i>Lower</i>	$10^{-6}$	$10^{-6}$	$10^{-6}$	589	$10^{-6}$	$10^{-6}$	$10^{-6}$	$10^{-6}$	1		
<b>3SR</b>	0.0769	0.0109	-	589	752	1,289	-	0.4746	2.4559	-	7/83
<b>4PR</b>	0.0208	0.0025	0.0613	589	1,078	37,220	387	0.4701	2.4074	0.7150	6/42/748
<i>Upper</i>	0.3	0.3	0.3	589	1,800	74,200	1,100	1	5		

**Table 1:** The table presents the fitted parameter values obtained from PI pulse decay experiments by Joos et al. (2013). For calibration on PD pulse decay data, see Appendix C. It also shows the *Lower* and *Upper* search bounds for the optimization problem in (10) and (14), specifying the allowable range for each parameter (see Sections 2 and 3.1 for details on model parameters and the fitting procedure). The table includes the ratio of ocean to land biosphere pulse absorption ( $\mathbf{m}_O^{t_e}/\mathbf{m}_L^{t_e}$ ) and the dynamic timescales ( $\tau$ ), based on the hyperparameters  $\rho_1$ ,  $\rho_2$ , and  $\rho_3$ . These are set to  $10^{-2}$ ,  $10^{-4}$ , and 0.0 for the 3SR model, and to  $10^{-2}$ ,  $10^{-4}$ , and  $10^{-4}$  for the 4PR model. The ocean-to-land biosphere pulse absorption ratio is measured at  $t_e = 20$ , with the atmospheric equilibrium mass  $\tilde{\mathbf{m}}_A$  fixed at the PI value of 589 GtC.

where  $\mathbf{m}_A^t/\mathbf{m}_A^0$  is the ratio of atmospheric CO<sub>2</sub> masses (or concentrations) at time  $t$  relative to pre-industrial (PI) levels, and  $\mathcal{F}_{2 \times \text{CO}_2}$  denotes the net radiative forcing associated with a doubling of atmospheric CO<sub>2</sub> concentration. For our purposes, we assume  $\mathcal{F}_{4 \times \text{CO}_2} = 2\mathcal{F}_{2 \times \text{CO}_2}$ . In Figure A.1, we present both the CO<sub>2</sub> radiative forcing and the ratio of total forcing to CO<sub>2</sub> radiative forcing.<sup>11</sup> Based on these values, we select  $\kappa = 1.2$  as the scaling factor to represent CO<sub>2</sub> radiative forcing across different RCP simulations, as discussed in Section 4. For the atmospheric perturbation tests described in Section 4.1, which involve controlled simulations based solely on synthetic CO<sub>2</sub> perturbation scenarios, we use  $\kappa = 1$ .

<sup>11</sup>The data is freely available from the RCP Database (version 2.0) at <https://tntcat.iiasa.ac.at/RcpDb>.

PARAMETERS FOR TWO-LAYER ENERGY-BALANCE MODEL

	$C$ ( $\text{W yr m}^{-2} \text{K}^{-1}$ )	$C_0$ ( $\text{W yr m}^{-2} \text{K}^{-1}$ )	$\gamma$ ( $\text{W m}^{-2} \text{K}^{-1}$ )	$\lambda$ ( $\text{W m}^{-2} \text{K}^{-1}$ )	$\mathcal{F}_{4 \times \text{CO}_2}$ ( $\text{W m}^{-2}$ )
Multimodel mean	7.3	106	0.73	1.13	6.9
Standard deviation	1.1	62	0.18	0.31	0.9

**Table 2:** The parameters are derived from the two-layered energy balance model outlined by [Geoffroy et al. \(2013b,a\)](#), representing the global thermal characteristics of coupled atmosphere-ocean general circulation models within a two-layer energy balance framework.

## 4 Simulations

This section presents three sets of simulations to test and validate the climate emulator framework, which includes both the carbon cycle and temperature models discussed in Sections 2 and 3. The climate emulator configurations used in the experiments are:

- (i) 3SR: A three-reservoir emulator connecting the atmosphere, upper ocean, and lower ocean.
- (ii) 4PR: An extension of the 3SR model, adding the land biosphere as a parallel carbon pathway from the atmosphere.
- (iii) 4PR-X: A variation of the 4PR model with a time-dependent operator to adjust the land biosphere’s equilibrium state for land-use-related emissions.

In Section 4.1, we describe atmospheric perturbation tests designed to facilitate consistent experimental comparisons across models. Section 4.2 presents simulations of global  $\text{CO}_2$  concentrations and temperature changes using RCP emission scenarios 2.6, 4.5, 6.0, and 8.5 (see Figure 4). The implications of the emulator design choices within a dynamic economic model are studied later in

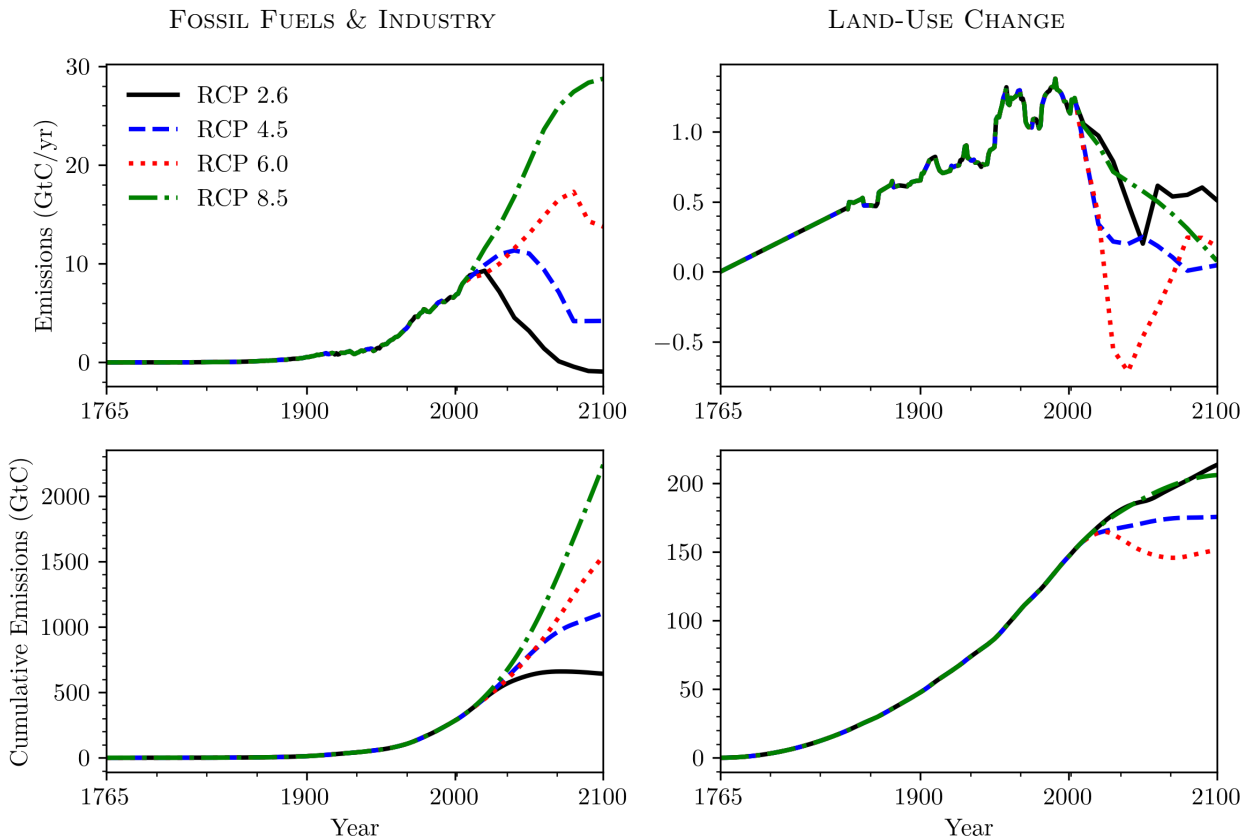


**Figure 4:** Yearly and cumulative  $\text{CO}_2$  emissions, showing total fossil fuel and industrial emissions (left column) and land-use-related emissions (right column).

Section 5.

## 4.1 Atmospheric Perturbation Tests

The initial experiment involves a pulse decay test to validate the atmospheric carbon decay trajectory, as discussed in Joos et al. (2013) and Zickfeld et al. (2021). Subsequently, we replicate the test outlined in MacDougall et al. (2020) to examine the emulator’s dynamics regarding zero-emission commitments. This experiment highlights key properties of the linear carbon cycle, particularly its scalar invariance and symmetry. These tests assess the strengths and limitations of the proposed climate emulator and enhance understanding of atmospheric carbon dynamics and their implications for climate conditions. Since land-use-related emissions are excluded, the 4PR-X climate emulator is not applicable here.

### 4.1.1 Pulse Decay:

This simulation models a 100 GtC carbon pulse introduced instantaneously into the atmosphere, with the system then allowed to evolve. The simulated pulse decay, using the 3SR and 4PR model configurations, is compared against pulse decay benchmarks discussed in Section 3.1. We also explore extreme dynamics by applying the weighted operator defined by  $-1 \leq \alpha \leq 1$  (see Section 3.1.2), where  $\alpha = 0$  represents mean dynamics, and  $\alpha = -1$  and  $\alpha = 1$  correspond to faster and slower pulse decay, associated with larger and smaller transfer rates, respectively. Simulated values are considered

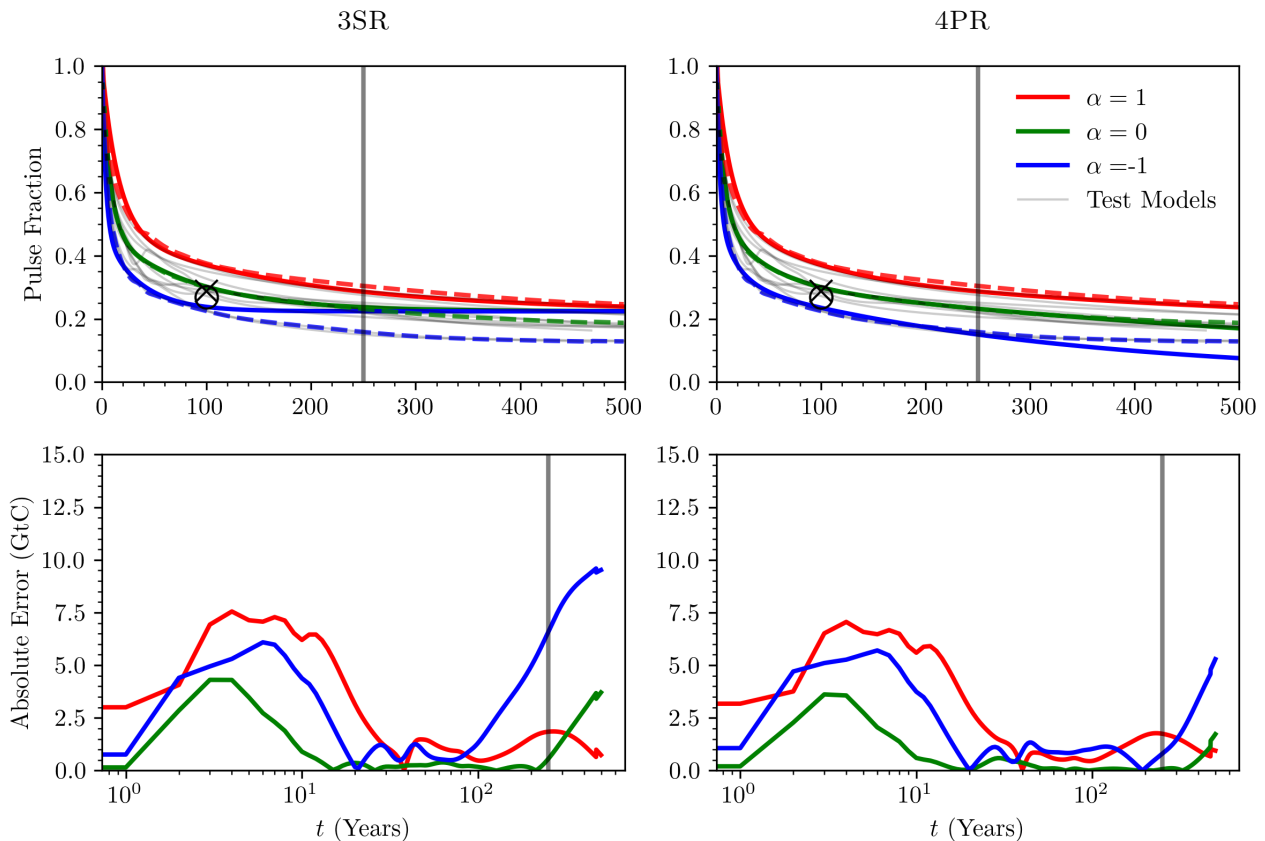


**Figure 5:** The figure displays the emulated pulse fraction and absolute error of a 100 GtC carbon pulse under pre-industrial (PI) conditions, assuming the carbon cycle is at equilibrium, for the 3SR (left column) and 4PR (right column) model configurations. Gray lines represent test model simulations from Joos et al. (2013), with dashed lines indicating the mean and two standard deviations. Solid lines show the results for different values of  $\alpha$ . Simulated values to the left of the vertical gray line at  $t = 250$  are in-sample, while those to the right are out-of-sample. The “x” and “○” markers indicate the 100 GtC and -100 GtC pulse fractions at  $t = 100$  from experiments by Zickfeld et al. (2021).

in-sample for  $t < 250$ , as they are used within the fitting procedure, while values for  $t \geq 250$  are treated as out-of-sample results, validating the model through predictive testing.

In Figure 5, we observe that for  $\alpha = 0$ , both the 3SR and 4PR configurations exhibit similar error metrics for  $t < 250$  when compared to the benchmark results of Joos et al. (2013). Figure B.2 shows the cumulative pulse absorption across different reservoirs. For  $t \geq 250$ , a significant difference emerges between the two model configurations. The primary distinction is that the 4PR model can represent short-, medium-, and long-term dynamic timescales  $\tau$ , while the 3SR model can only represent two timescales, namely short- and medium-term dynamics (see Table 1 for details). This limitation of the 3SR model becomes more pronounced for simulations with  $\alpha \neq 0$ . Overall, the 4PR configuration demonstrates improved accuracy over 3SR, particularly in the out-of-sample results.

The linearity of the carbon cycle model ensures homogeneity and symmetry, meaning that the fraction of the pulse remains consistent regardless of pulse magnitude. As a result, pulse emissions of 1000, 100, or  $-100$  GtC all follow the trajectory shown in Figure 5. However, this does not accurately reflect real-world dynamics. In an extreme case, for example, carbon reservoirs cannot be depleted beyond 100% of their original mass, yet they can increase by more than that. Zickfeld et al. (2021) highlighted this asymmetry in various tests using the UVic ESCM 2.9 model, where the fraction of the  $\pm 100$  GtC pulses remaining in the atmosphere is annotated in Figure 5. Although relatively small for a 100 GtC pulse, this asymmetry becomes more pronounced as the magnitude of the introduced pulse increases.

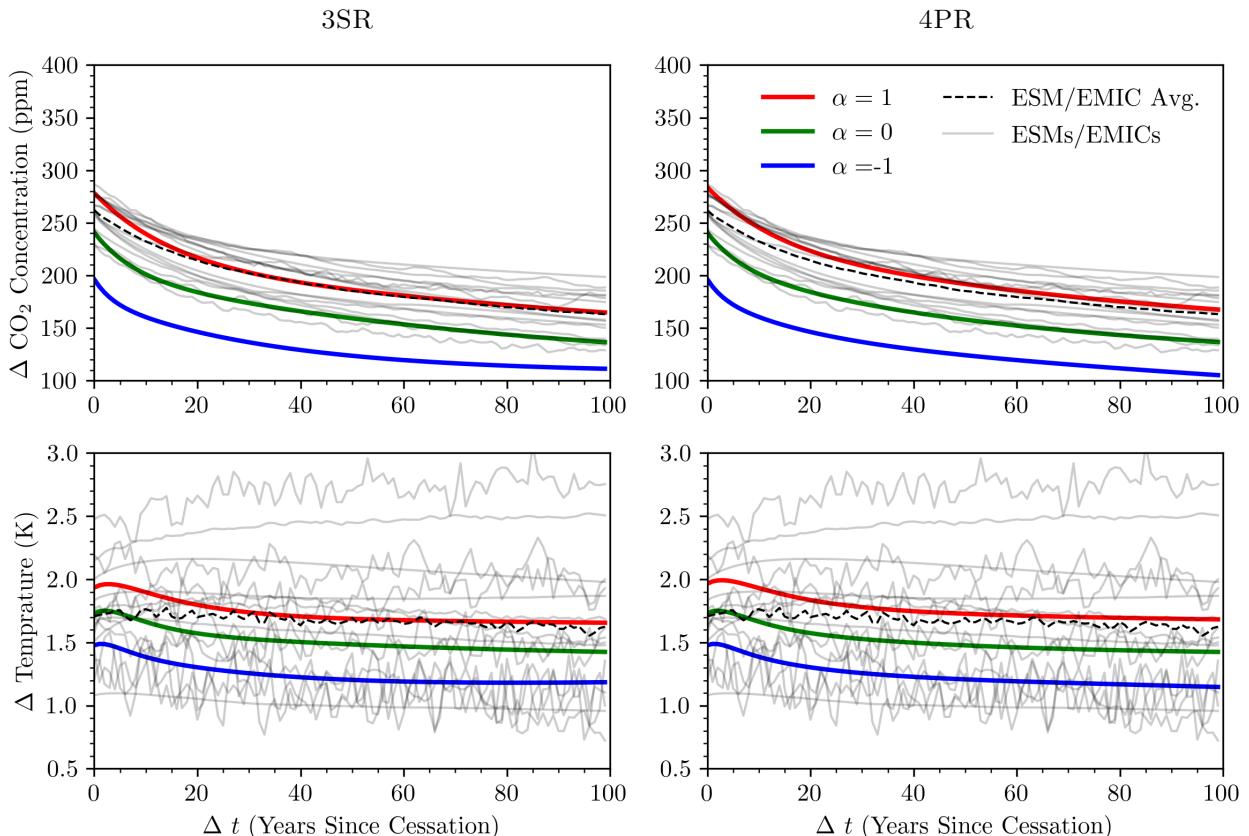


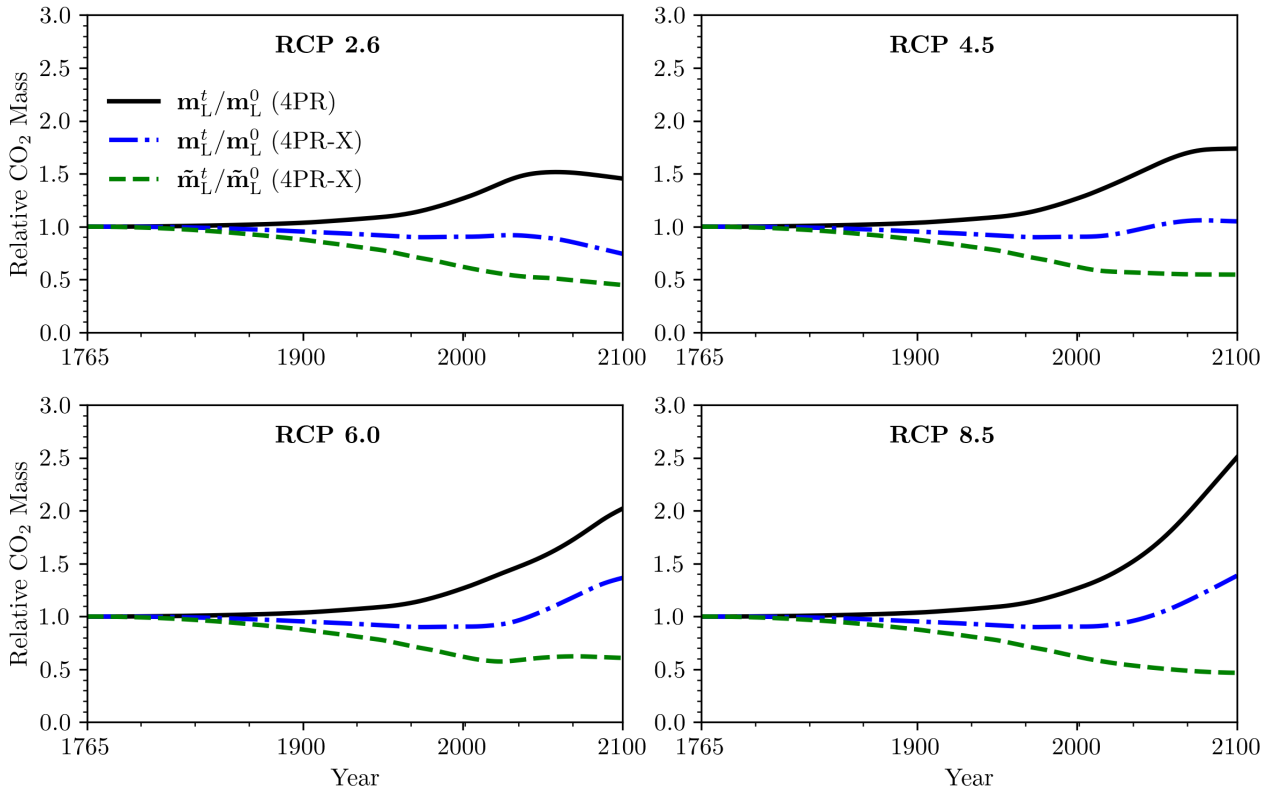
**Figure 6:** The simulated changes in atmospheric CO<sub>2</sub> concentrations and temperatures following the cessation event are shown for the 3SR (left column) and 4PR (right column) model configurations. The three thick solid lines represent the model-simulated changes in concentrations and temperatures for different values of  $\alpha$ . Thin solid lines show simulations from MacDougall et al. (2020) using ESMs and EMICs, with the dashed thin line indicating the average across these simulations.

#### 4.1.2 Zero Emissions:

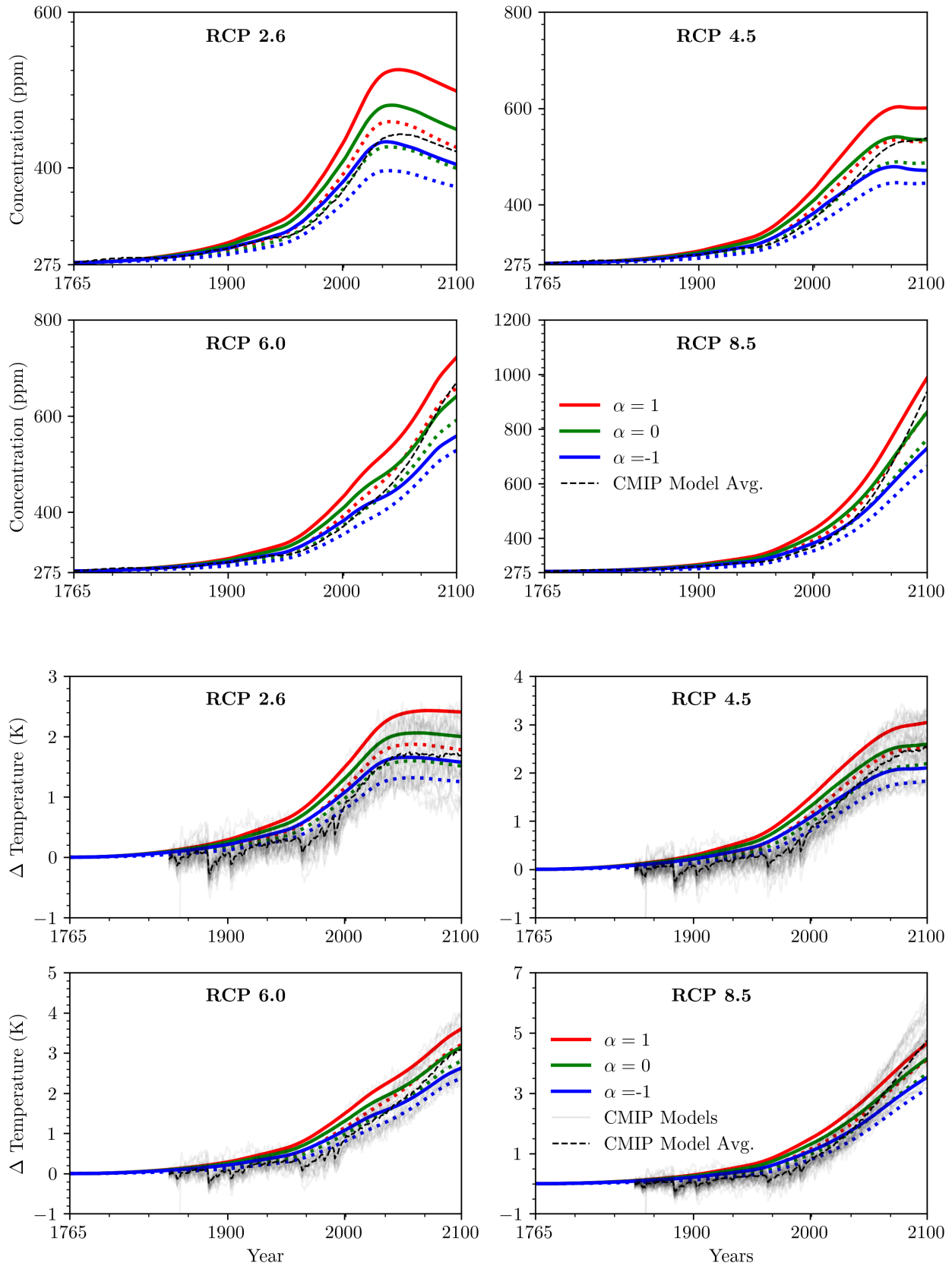
This numerical experiment follows the protocol of the Zero Emissions Commitment Model Intercomparison Project (ZECMIP), which aims to quantify unrealized temperature change after CO<sub>2</sub> emissions cease (MacDougall et al., 2020). The exercise begins with CO<sub>2</sub> emissions increasing atmospheric concentrations by 1% per year until cumulative emissions reach 1000 GtC. At this cessation point, no further CO<sub>2</sub> emissions are introduced, and the model evolves freely.

Figure 6 shows the simulated changes in atmospheric CO<sub>2</sub> concentration and global mean temperature after cessation, along with ESM and EMIC simulations for comparison. Additional details are provided in Figure B.3, which displays cumulative emissions absorption by different reservoirs in each model configuration.

From Figure 6 it can be taken that the box-model succeeds in emulating the overall decay of the atmospheric carbon concentration after cessation of the emissions. The 4PR model, which offers one more free parameter or characteristic decay time scale than the 3SR model, reproduces the multi-model mean time evolution of the ESMs and EMICs (black dashed curve). Also apparent is a general limitation of any linear carbon cycle model. Lacking the ability to emulate any non-linear feedbacks, notably the carbon-climate and carbon-concentration feedbacks (Joos et al., 2013; Arora et al., 2020), a linear CCE under a strong emission scenario will either under- or over-estimate atmospheric carbon concentration. In Figure 6, the obvious underestimation of atmospheric carbon content at time zero (the green curve lying below the black dashed curve) is due to the fact that the CCE is calibrated under PI background conditions, where reservoir contents are such that carbon quickly leaves the atmosphere and the pulse decays more rapidly and more strongly than if the CCE were calibrated under PD conditions.



**Figure 7:** The current and equilibrium masses of the land biosphere, denoted as  $m_L^t$  and  $m_{\tilde{L}}$ , respectively, are shown as fractions of their initial values. Results are provided for both constant and time-dependent simulations across each RCP scenario. Initial equilibrium conditions are based on the PI calibration values listed in Table 1. These results pertain specifically to the 4PR land biosphere model, where the ratio  $m_L^t/m_{\tilde{L}}^t$  is relevant only in time-dependent operator simulations, equating to 1 in constant operator simulations.



**Figure 8:** The figures show simulation results for atmospheric CO<sub>2</sub> concentrations and temperature changes using the 3SR and 4PR model configurations. We compare the *constant operator* test (dotted lines) with the *time-dependent operator* in the 4PR model (solid line) for different values of  $\alpha$ , starting from PI conditions. In the time-dependent operator simulation, land biosphere equilibrium masses are adjusted based on land-use-related emissions, as shown in Figure 7.

## 4.2 Representative Concentration Pathway

Figure 7 presents the changes in land biosphere carbon mass relative to PI conditions (i.e., at  $t = 0$ ) across different RCP scenarios for the 4PR and 4PR-X models. Yearly and cumulative emissions are also shown in Figure 7. The 4PR-X model exhibits a reduction in absorbed carbon,  $\mathbf{m}_L^t$ , compared to 4PR, due to the reduced equilibrium mass of the land biosphere,  $\tilde{\mathbf{m}}_L^t$ , in 4PR-X, supporting our initial assertions in Section 2.2. The relative land-biosphere carbon content,  $\mathbf{m}_L^t/\mathbf{m}_L^0$ , remains roughly constant in time for the 4PR-X model, in line with observation-based estimates (Ciais et al., 2014), whereas the 4PR model features a distinct increase.

Atmospheric concentrations and global temperature changes under RCP emissions scenarios are shown in Figure 8. In previous simulations, the 4PR model configuration demonstrated a more accurate capture of long-term pulse decay dynamics than the 3SR model. However, this has minimal impact on the RCP simulations, as the results for both 4PR and 3SR are indistinguishable (dotted lines in Figure 8). In contrast, higher concentrations and temperature changes are observed in simulations with the 4PR-X model. Focusing on tests with the weighted operator parameter  $\alpha = 0$  (see Section 3.1.2) and comparing these results with CMIP model averages for atmospheric concentrations and temperature changes, we find that the 4PR-X model closely aligns with the less extreme RCP scenarios 4.5 and 6.0. These findings underscore the influence of equilibrium mass changes in the land biosphere on global temperature modeling. For RCP 2.5 and 8.0, representing emissions significantly lower and higher than current levels, CMIP model averages for 2100 concentrations and temperatures are best approximated by  $\alpha = -1$  for RCP 2.5 and  $\alpha = 1$  for RCP 8.0. These results demonstrate that adjusting  $\alpha$  can effectively model more extreme scenarios, with lower and higher values of  $\alpha$  corresponding to plausible lower and higher atmospheric carbon concentrations, respectively.

## 5 Economic Implications of Carbon Cycle Models

To examine the implications of different carbon cycles on macroeconomic indicators, we use an economy-climate model based on the well-known and well-studied DICE-2016 framework (Nordhaus, 2017) and the climate emulator developments presented above. We consider three climate emulators introduced in Section 2 and explored further in Sections 4.1 and 4.2, following the paper’s notation: 3SR, 4PR, and 4PR-X.<sup>12</sup>

Our primary goal in this section is to understand whether utilizing these different climate emulators within an economy-climate setup has significant economic implications. We will show that the choices made in constructing a customized emulator are not always inconsequential. These analyses serve as an initial exploration of models with additional carbon reservoirs. We consider these illustrative results as a starting point for further research on the applications and limitations of climate-economy models with richer climate emulators. Based on the results below, we aim to offer preliminary recommendations on when it is appropriate to use a climate emulator with extra reservoirs and possibly dynamic feedback in equilibrium mass (also referred to as the model with a time-dependent operator).<sup>13</sup>

The economic model used for our exploratory studies consists of a single, infinitely lived, representative consumer and a single firm. We describe the equilibrium allocation as the solution to a social planner problem where the planner maximizes a constant relative risk aversion (CRRA) utility function of per capita consumption,  $C_t/L_t$ . Here,  $C_t$  represents consumption,  $L_t$  denotes labor, with a constant intertemporal elasticity of substitution (IES),  $\psi > 1$ , and a discount factor,  $0 < \beta < 1$ .<sup>14</sup>

<sup>12</sup>Recall that a more detailed description of the carbon cycles under consideration can be found in Section 2, and energy balance equations are presented in Section 3.2.

<sup>13</sup>All IAMs discussed below were solved using “Deep Equilibrium Nets,” a deep learning-based global solution method for dynamic stochastic models. For a general introduction to this method, see Azinovic, Gaegauf, and Scheidegger (2022), and for its application in the context of IAMs, refer to Friedl et al. (2023).

<sup>14</sup>In the online Appendix D, we list all exogenous variables, equations, and parameters of the model.

The value of the lifetime utility,  $V_0$  is given by the following expression:

$$V_0 = \max_{\{C_t, \mu_t\}_{t=0}^{\infty}} \sum_{t=0}^{\infty} \beta^t \frac{\left(\frac{C_t}{L_t}\right)^{1-1/\psi} - 1}{1 - 1/\psi} L_t \quad (18)$$

$$\text{s.t. } K_{t+1} = (1 - \Theta(\mu_t) - \Omega(T_t^{\text{AT}})) K_t^\alpha (A_t L_t)^{1-\alpha} + (1 - \delta)K_t - C_t \quad (19)$$

Climate Eqs. (1), (16) and (17)

$$0 \leq K_{t+1} \quad (20)$$

$$0 \leq \mu_t \leq 1 \quad (21)$$

where emissions that enter (1) are defined as follows with  $E_t^{\text{Land}}$  being exogenous land emissions:

$$e^t = \sigma_t Y_t^{\text{Gross}}(A_t, K_t, L_t)(1 - \mu_t) + E_t^{\text{Land}}. \quad (22)$$

Output  $Y_t^{\text{Gross}}(A_t, K_t, L_t)$  is produced using a Cobb-Douglas technology, with capital  $K_t$ , total factor productivity (TFP)  $A_t$ , and labor  $L_t$ , where  $\alpha$  represents capital elasticity. The capital stock depreciates at rate  $\delta$ . Mitigation efforts, denoted by rate  $\mu_t$ , are costly and reduce output by a factor  $\Theta(\mu_t)$ . Additionally, higher temperatures decrease output through the damage function  $\Omega(T_t^{\text{AT}})$  where  $T_t^{\text{AT}}$  denotes atmospheric temperature. For a detailed specification and parameterization of all equations, including exogenous variables, damages, and the procedure for integrating the climate emulator up to present-day conditions, please refer to the online Appendix C.

We first consider the business-as-usual (BAU) case, where the social planner does not invest in mitigation  $\mu_t$ . In this scenario, the planner only chooses the investment sequence, setting the mitigation sequence to zero at all times. Next, we consider the optimal mitigation case, where the planner simultaneously chooses investment in both capital and mitigation. In both cases, we examine the social cost of carbon, defined as the marginal cost of atmospheric carbon in terms of the numeraire good. Following the literature (see, e.g., Traeger (2014) and Cai and Lontzek (2019)), we define the SCC as the planner's marginal rate of substitution between atmospheric carbon concentration and the capital stock:

$$SCC_t = -\frac{\partial V_t / \partial M_{\text{AT},t}}{\partial V_t / \partial K_t}. \quad (23)$$

The SCC equals the optimal carbon tax when  $\mu_t < 1$ .

In the following sections, we examine benchmark solutions for both the BAU (Section 5.1) and optimal mitigation cases (Section 5.2). We then assess emulator performance under a hypothetical carbon capture and storage technology (Section 5.3). Additionally, we analyze result sensitivity to damages and discount rates, with details in Appendix E. Results for present-day simulations are provided in Appendix C.

## 5.1 Business-As-Usual

We begin by examining the results for the BAU case across the carbon cycle models presented above. In this and subsequent figures, the 3SR model is represented by a solid red line, the 4PR model by a solid green line, and the 4PR-X model by a dashed green line.<sup>15</sup> In Figure 9 (top left panel), we observe that industrial emissions are identical across all carbon cycle models. However, the carbon mass in the land biosphere (Figure 9, top right panel) and atmosphere (Figure 9, bottom left panel) differ between the 4PR and 4PR-X models. This variation arises because the dynamic 4PR-X model simulates a decreasing land biosphere capacity, which leads to increased carbon uptake by other reservoirs, thereby raising atmospheric carbon mass and, consequently, temperature (Figure 9, bottom

<sup>15</sup>Differences in the initial values of the land biosphere reservoir stem from the climate emulator's integration procedure up to present-day conditions. For details, refer to Appendix D.

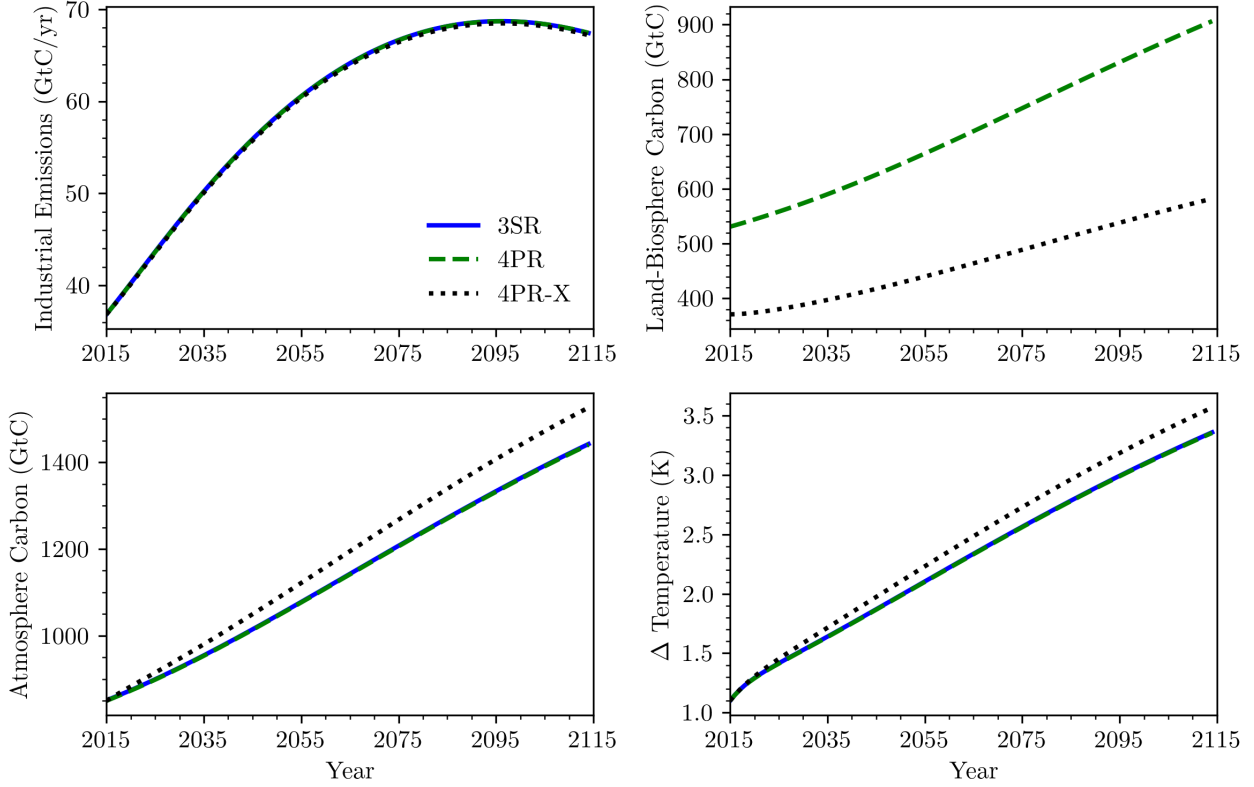


**Figure 9:** The simulation results for the BAU case ( $\mu_t = 0$ ).

right panel). The rather low carbon content of the land reservoir of the 4PR-X model in the year 2015 (below 400 GtC and thus slightly outside the estimated range in [Ciais et al. \(2014\)](#)) is linked to the fact that we chose to simply remove all land-use change emissions from the land biosphere equilibrium mass instead of applying some scaling as discussed in Section 2.2.

Table 3 presents the exact values for atmospheric carbon mass and temperature in 2020, 2050, and 2100, along with the percentage differences between the 3SR and 4PR-X models.

Year	Variable	3PR (1)	4PR (2)	4PR-X (3)	diff (1) & (3)
2020	$M_{2020}^{\text{AT}}$	874.37	873.52	883.14	1.00%
2050	$M_{2050}^{\text{AT}}$	1046.07	1045.01	1085.54	3.77%
2100	$M_{2100}^{\text{AT}}$	1363.19	1361.66	1439.97	5.63%
2020	$T_{2020}^{\text{AT}}$	1.29	1.29	1.30	0.99%
2050	$T_{2050}^{\text{AT}}$	1.99	1.98	2.10	5.84%
2100	$T_{2100}^{\text{AT}}$	3.09	3.09	3.29	6.34%

**Table 3:** Data for atmospheric carbon mass ( $M_t^{\text{AT}}$ ) and atmospheric temperature ( $T_t^{\text{AT}}$ ) across selected years.

In the BAU case, the carbon masses and temperatures in 2020 show no significant variation across the different carbon cycle models. However, by 2050, differences become substantial: the dynamic 4PR-X model shows nearly 4% higher atmospheric carbon and approximately 6% higher atmospheric temperature than the 3SR model. This 6% temperature increase in the 4PR-X model corresponds to an 11% higher economic loss, equivalent to approximately 0.5 trillion USD (2015 value).

## 5.2 Optimal Mitigation

In Figure 10, we examine the evolution of the same variables under optimal mitigation. Overall, the relative dynamics of the 4PR-X model compared to the 3SR and 4PR models remain consistent with the BAU case. In the optimal scenario, we also include the mitigation rate and the SCC, as shown in the bottom-right panel of Figure 10. As expected, both mitigation and SCC are higher in the 4PR-X dynamic model than in the static 3SR and 4PR models, in line with the temperature dynamics. Exact numerical values and percentage differences are provided in Table 4 where we observe that, in 2020, the SCC in the 4PR-X model exceeds that of the 3SR model by 11.9%, increasing to 13.9% by 2050.

The benchmark analysis shows no performance difference between models with three versus four reservoirs, as adding a land biosphere reservoir does not affect outcomes in the BAU case or optimal mitigation. However, introducing dynamics in the four-reservoir model, where the equilibrium mass of the land biosphere declines over time, results in higher temperature increases in the BAU case

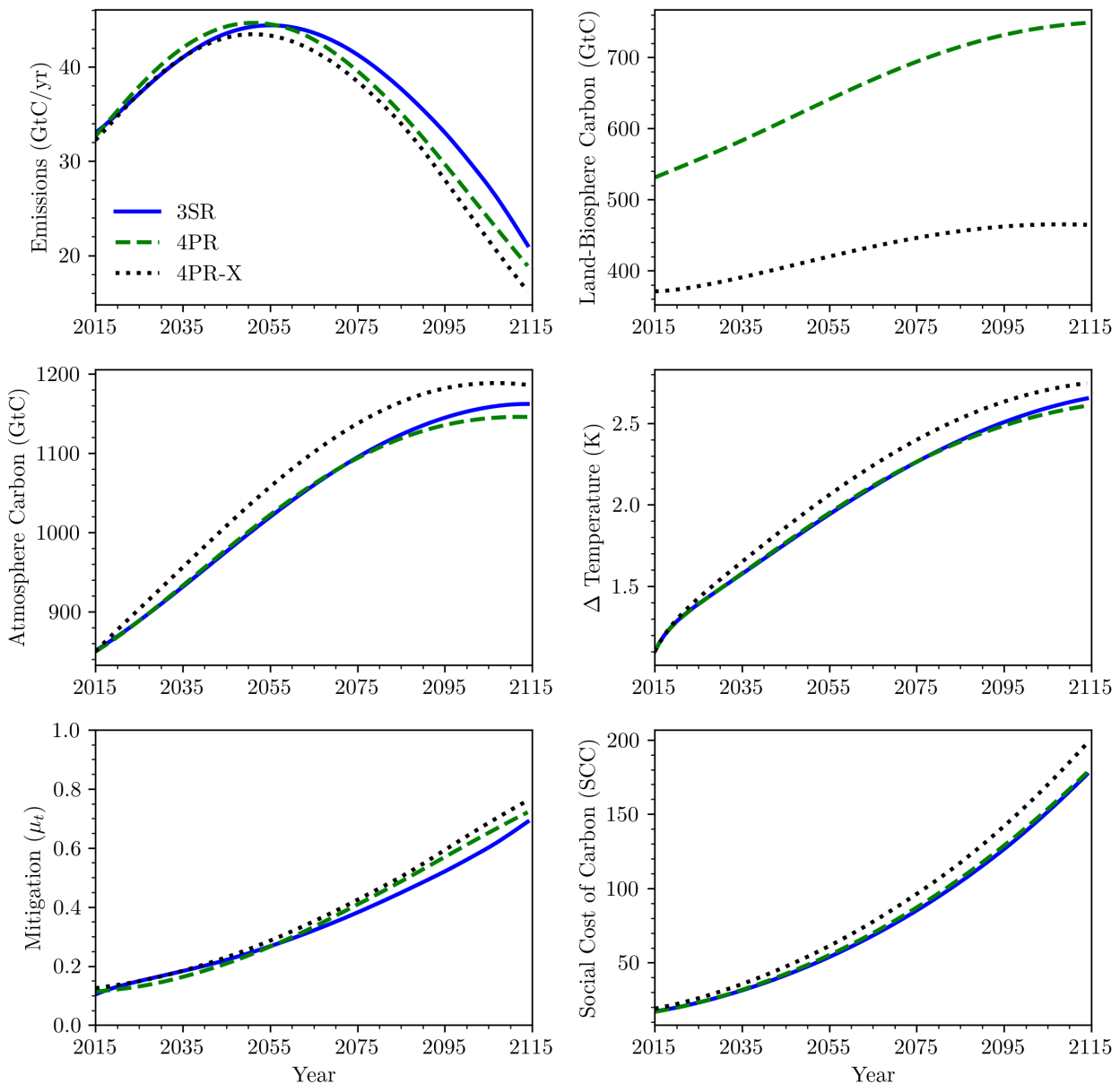


**Figure 10:** Simulation results for the optimal abatement scenario.

Year	Variable	3PR (1)	4PR (2)	4PR-X (3)	diff (1) & (3)
2020	SCC	19.85	19.72	22.20	11.87%
2050	SCC	47.47	48.57	54.07	13.90%
2100	SCC	138.58	140.82	155.45	12.18%

**Table 4:** Social Cost of Carbon data across different years.

compared to static models. Additionally, incorporating deforestation processes leads to a higher SCC, indicating that deforestation modeling substantially impacts policy outcomes. These findings suggest that accounting for deforestation requires a higher carbon tax to effectively mitigate climate change impacts.

### 5.3 Carbon Capture & Storage

We now try to mimic a carbon capture and storage type of research question within the DICE-2016 framework to illustrate that the choices made in a climate emulator are not always innocuous. We model this setting in a very stylized fashion by assuming that a mitigation rate for the emissions is equal to unity starting from the initial period. This implies that industrial emissions are no longer entering the atmosphere. The dynamics of the mass of carbon in the atmosphere and the atmospheric temperature for the carbon cycles under consideration are presented in Figure 11. The exact numerical values for the atmospheric temperature are given in Table 5.

Year	Variable	3PR (1)	4PR (2)	4PR-X (3)	diff (1) & (3)
2020	$T_{2020}^{AT}$	1.22	1.22	1.23	0.89%
2050	$T_{2050}^{AT}$	1.14	1.14	1.22	6.72%
2100	$T_{2100}^{AT}$	1.10	1.10	1.18	7.09%

**Table 5:** Atmospheric temperature data ( $T_t^{AT}$ ) across different years.

As in the BAU and optimal cases, adding a static land biosphere reservoir does not alter the evolution of climate variables. However, the dynamic model shows similar patterns observed in the BAU and optimal cases. This suggests that, with carbon capture and storage technologies implemented alongside ongoing deforestation, temperature trajectories could be approximately 7% higher by 2050.

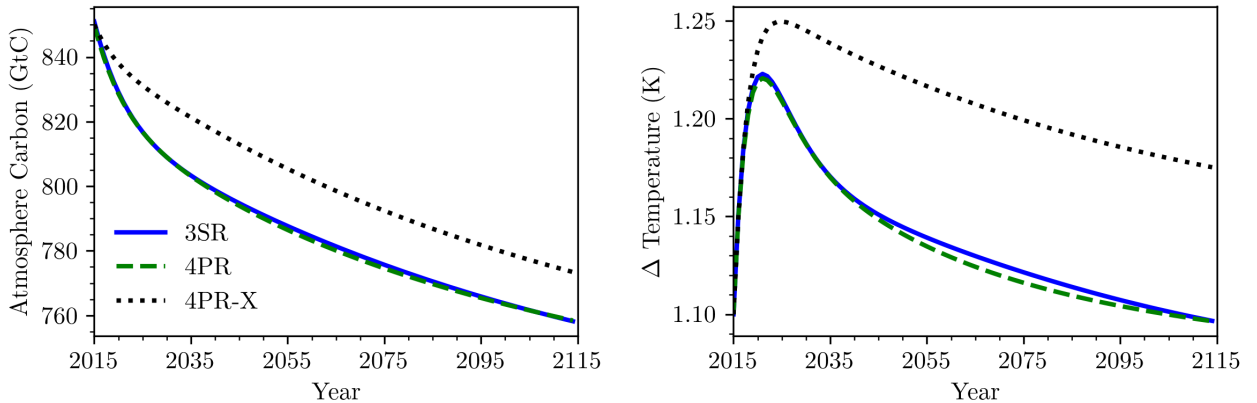


**Figure 11:** Atmospheric carbon concentrations (left panel) and atmospheric temperature (right panel) under the full abatement scenario ( $\mu_t = 1$ ).

## 6 Conclusion

This paper develops and evaluates an adaptable computational framework that empowers any IAM modeler—even those without specialized training in climate science—to construct interpretable and computationally efficient custom-built climate emulators tailored to their specific research questions. The flexibility of our framework allows for the construction and calibration of box-model-type climate emulators that better represent potential policy-relevant scenarios. By focusing on linear box-model emulators, we offer a transparent and interpretable approach that enables seamless integration and accurate calibration of custom climate dynamics within economic and policy analyses of climate change.

Our results indicate that climate emulators with an additional land biosphere reservoir significantly enhance climate-economic simulations, especially when dynamic land-use changes are taken into account. The 4PR model, which incorporates the land biosphere as an explicit reservoir, and the 4PR-X model, which additionally accounts for land-use dynamics such as deforestation, exhibit distinct patterns in atmospheric CO<sub>2</sub> and temperature outcomes under Representative Concentration Pathways (RCPs) and business-as-usual (BAU) scenarios. The 4PR-X model, in particular, shows a pronounced sensitivity to land-use changes, resulting in higher atmospheric carbon concentrations and temperatures. In contrast, the 4PR, with a static land-biosphere storage capacity, produces outcomes similar to the 3SR model, which lacks a separate land-biosphere reservoir altogether. Our findings underscore the importance of integrating the land biosphere with a dynamically calibrated carbon storage capacity into climate emulators to improve the accuracy of climate change impact assessments.

Our analysis also emphasizes the economic implications of different climate emulators. In scenarios with optimal mitigation, the social cost of carbon is notably higher when the dynamic land biosphere model (4PR-X) is used, implying that stronger policy responses to control emissions are warranted in the presence of deforestation and urbanization processes. Furthermore, the carbon capture and storage analysis suggests that ignoring land-use changes in climate emulators may lead to underestimating projected atmospheric CO<sub>2</sub> levels and temperatures. Therefore, in cases where land management practices play a significant role, our framework’s models highlight the necessity for higher carbon taxation or equivalent policy interventions to offset these effects.

In sum, our work advances the current literature by providing a comprehensive, customizable framework for building climate emulators for IAMs. This work is complemented by a comprehensive code framework that can be accessed online at [https://github.com/ClimateChangeEcon/Building\\_Interpretable\\_Climate\\_Emulators\\_forEconomics](https://github.com/ClimateChangeEcon/Building_Interpretable_Climate_Emulators_forEconomics). Future research can extend this framework to explore nonlinear interactions between carbon reservoirs, further enhancing its applicability to a broader set of policy questions. We envision this framework to serve as a versatile tool for economists and policymakers seeking to design and assess climate policies that reflect the complexities of land biosphere dynamics.

## A Explicit Carbon and Temperature Model Definition

The equations defining the carbon cycle dynamics for the 4PR reservoir are presented in detail below. These are equivalent to the matrix formulation provided in Section 2. Notice that the fitting procedure is described in Section 3.1 and the results are shown in Table 1 where  $\mathbf{A}_{2,1} := \mathbf{a}_{A \rightarrow O_1}^\mu$ ,  $\mathbf{A}_{3,2} := \mathbf{a}_{O_1 \rightarrow O_2}^\mu$ ,  $\mathbf{A}_{4,1} := \mathbf{a}_{A \rightarrow L}^\mu$ . The 3SR carbon cycle can be derived from the same equation by setting  $\mathbf{A}_{4,1} = 0$ . The system of equations described in (1) can be expressed as follows:

$$\begin{aligned} \mathbf{m}_A^{t+1} &= (1 - \mathbf{A}_{2,1} - \mathbf{A}_{4,1}) \cdot \mathbf{m}_A^t + \mathbf{A}_{2,1} \cdot \frac{\tilde{\mathbf{m}}_A}{\tilde{\mathbf{m}}_{O_1}} \cdot \mathbf{m}_{O_1}^t + \mathbf{A}_{4,1} \cdot \frac{\tilde{\mathbf{m}}_A}{\tilde{\mathbf{m}}_L} \cdot \mathbf{m}_L^t \\ \mathbf{m}_{O_1}^{t+1} &= \mathbf{A}_{2,1} \cdot \mathbf{m}_A^t + \left(1 - \mathbf{A}_{2,1} \cdot \frac{\tilde{\mathbf{m}}_A}{\tilde{\mathbf{m}}_{O_1}} - \mathbf{A}_{3,2}\right) \cdot \mathbf{m}_{O_1}^t + \mathbf{A}_{3,2} \cdot \frac{\tilde{\mathbf{m}}_{O_1}}{\tilde{\mathbf{m}}_{O_2}} \cdot \mathbf{m}_{O_2}^t \\ \mathbf{m}_{O_2}^{t+1} &= \mathbf{A}_{3,2} \cdot \mathbf{m}_{O_1}^t + \left(1 - \mathbf{A}_{3,2} \cdot \frac{\tilde{\mathbf{m}}_{O_1}}{\tilde{\mathbf{m}}_{O_2}}\right) \cdot \mathbf{m}_{O_2}^t \\ \mathbf{m}_L^{t+1} &= \mathbf{A}_{4,1} \cdot \mathbf{m}_A^t + \left(1 - \mathbf{A}_{4,1} \cdot \frac{\tilde{\mathbf{m}}_A}{\tilde{\mathbf{m}}_L}\right) \cdot \mathbf{m}_L^t. \end{aligned} \quad (24)$$

The temperature model and its parameters are detailed in Section 3.2, with explicit definitions for the temperatures of the atmosphere and upper ocean provided below:

$$\begin{aligned} \mathbf{x}_A^{t+1} &= \mathbf{x}_A^t + \frac{1}{C} \left( \kappa \cdot \frac{\mathcal{F}_{2 \times \text{CO}_2}}{\ln(2)} \cdot \ln \left( \frac{\mathbf{m}_A^t}{\mathbf{m}_A^0} \right) - \gamma \cdot (\mathbf{x}_A^t - \mathbf{x}_{O_1}^t) - \lambda \cdot \mathbf{x}_A^t \right) \\ \mathbf{x}_{O_1}^{t+1} &= \mathbf{x}_{O_1}^t + \frac{\gamma}{C_0} (\mathbf{x}_A^t - \mathbf{x}_{O_1}^t) \end{aligned} \quad (25)$$

We scale the  $\text{CO}_2$  relative forcing by a factor of  $\kappa = 1.2$  for various RCP simulations, based on estimates from the data in Figure A.1, which displays the ratio of total forcing to  $\text{CO}_2$  radiative forcing. For the atmospheric perturbation tests detailed in Section 4.1, involving controlled simulations based exclusively on synthetic  $\text{CO}_2$  perturbation scenarios, we set  $\kappa = 1$ .

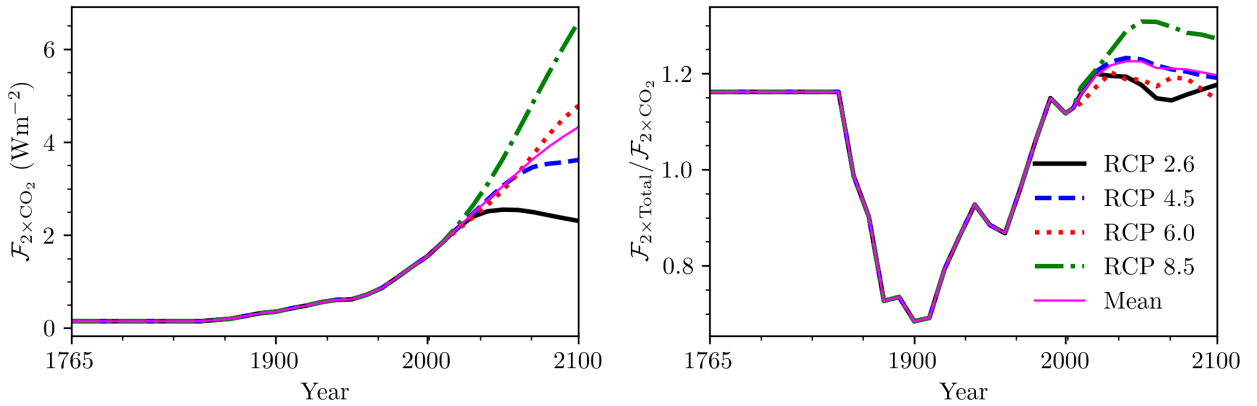


**Figure A.1:** A visualization of the  $\text{CO}_2$  radiative forcing parameter  $\mathcal{F}_{2 \times \text{CO}_2}$  (left) and the ratio of total to  $\text{CO}_2$  forcing (right) across various RCP scenarios from PI times to 2100. The mean value across RCP scenarios is shown as the thin solid pink line.

## B Extended Results

**Pulse Decay** Figure B.1 and B.2 are simulation based on a 100 GtC pulse decay. The model used for this simulation is discussed in detail in Sections 2 and 3. The results show the fraction of the pulse absorbed by different reservoirs in the 3SR and 4PR model configurations. Here,  $O_2$ ,  $O_1$ , and L represent the upper ocean, deep ocean, and land biosphere reservoirs, respectively, with the dashed red line indicating the  $\mu$ -benchmark for the remaining carbon mass. The experiment is based on PI conditions starting from 1765, with a dashed red line serving as the benchmark simulation derived from various test models of differing complexities (for further details, see Joos et al. (2013)). The vertical gray line marks the time span of 250 years used for fitting the model parameters. Note that the simulation results to the left and right of this line correspond to in-sample and out-of-sample results, respectively. The pink vertical line signifies the 20-year mark at which the  $q_1$  penalty function enforces an approximately equal mass of carbon absorption between the oceans and the land biosphere. Note that the  $q_1$  penalty function is only relevant in the 4PR model configuration.

**Zero Emissions** Figure B.3 presents results from the experiments outlined in Section 4.1, following the Zero Emissions Commitment Model Intercomparison Project (ZECMIP) protocol (MacDougall et al., 2020). These experiments examine the impact of carbon emissions and subsequent zero-emission states on climate variables over time. The results correspond to a *Type A* test, where simulations begin under PI conditions and emissions are introduced to achieve a 1% increase in atmospheric carbon concentration per year until total emissions reach 1000 GtC. At this point, symbolized by the gray vertical line, emissions cease, and the system evolves without further carbon inputs. Note that the cessation point varies across simulations. We also denote the atmosphere as A in the ‘‘Pulse Decay’’ description. Results are shown for the weighted operator  $\mathbf{A}^\alpha$  with  $\alpha = 1, 0$ , and  $-1$ , as described in Section 3.

**RCP** Figure B.4 shows changes in reservoir mass relative to PI conditions for the RCP experiments detailed in Section 4.2. Displayed are the multimodal mean-fitted model parameters for  $\alpha = 0$ , specifically comparing the 4PR model with a *constant operator* to the 4PR-X model with a *time-dependent operator*. The 3SR model demonstrates behavior closely resembling the 4PR simulation with a constant operator, except for the fact that in the 3SR model, the carbon typically stored in the land biosphere is instead absorbed by ocean reservoirs.

## PULSE DECAY: EFFECTS PENALTY FUNCTIONS

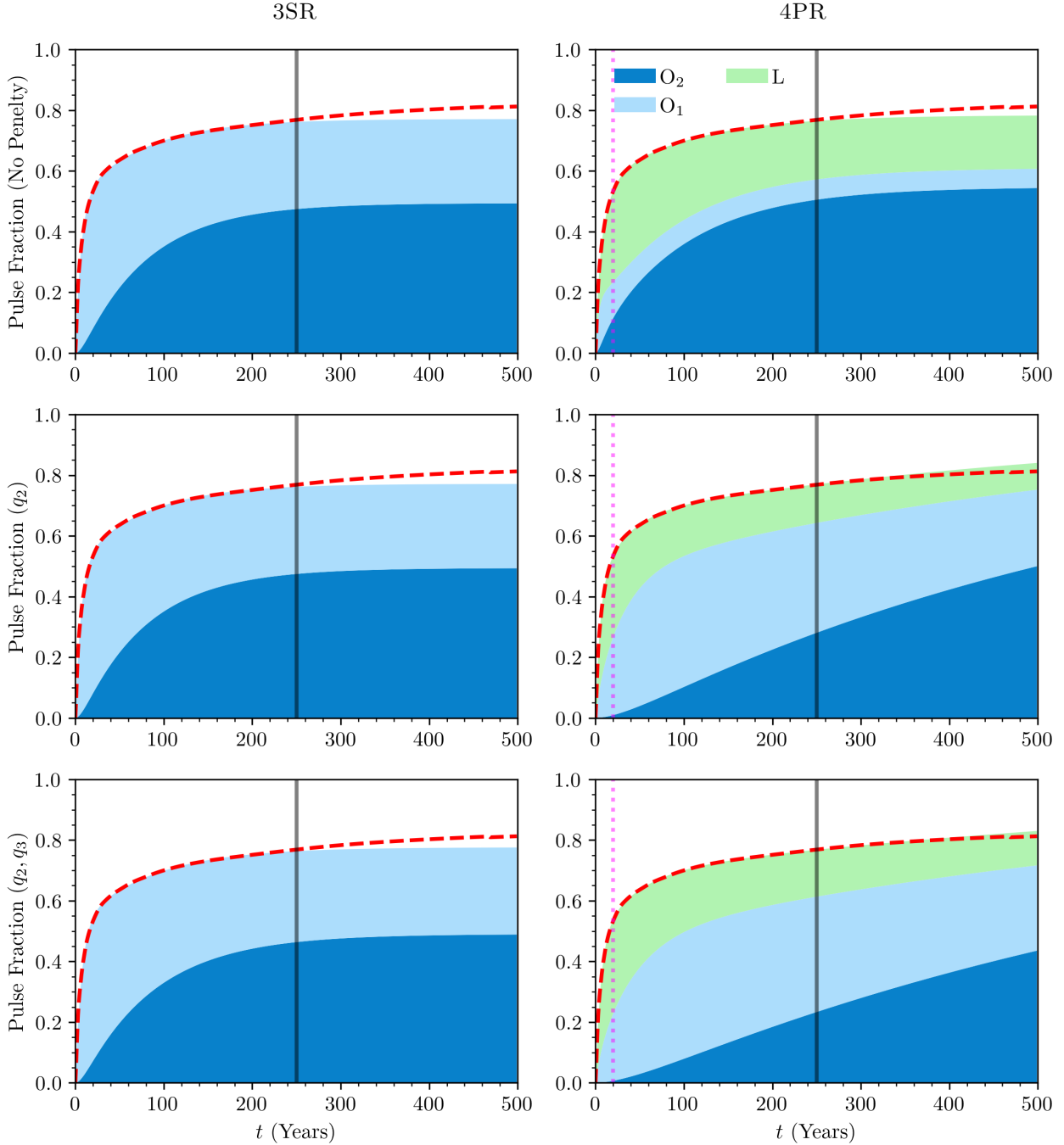


**Figure B.1:** The figure illustrates the effect of the penalty functions for “Equilibrium Mass Variability” ( $q_2$ ) and “Reservoir Absorption Ratios” ( $q_3$ ) on the simulated relative mass of a 100 GtC pulse remaining in the atmosphere over a 500-year period for the 3SR (left column) and 4PR (right column) model configurations. The simulation setup follows the descriptions provided in Section 3, with specific details in Section 3.1.1.

## PULSE DECAY: FITTED MODEL RESERVOIR ABSORPTION

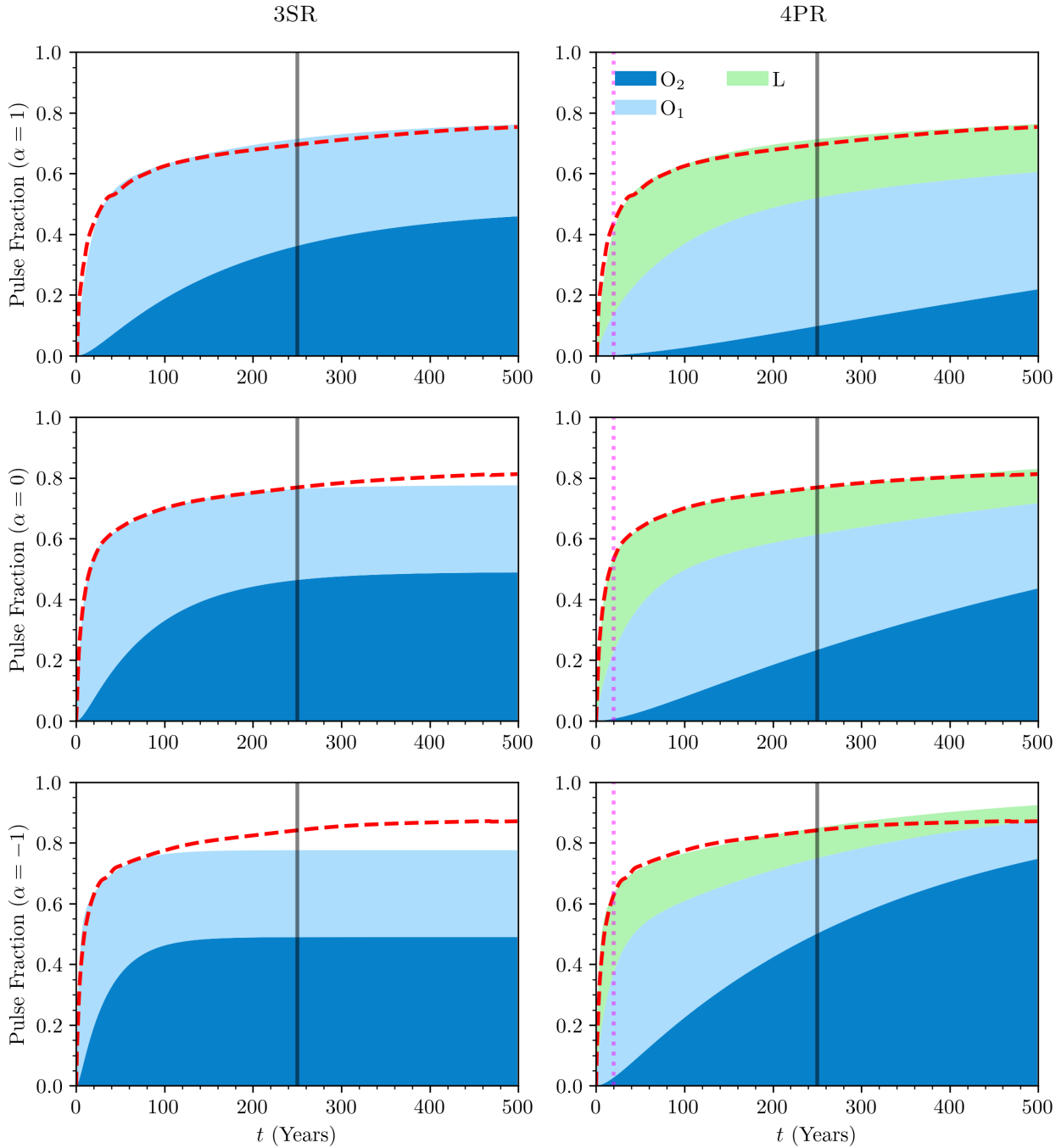


**Figure B.2:** The figure displays the fraction of a 100 GtC pulse absorbed by various reservoirs over a 500-year period using the weighted operator  $\mathbf{A}^\alpha$  for the 3SR (left column) and 4PR (right column) model configurations; see Section 3.1.2 for further details. The benchmark simulation with  $\alpha = 0$  represents the mean benchmark model ( $\mu$ -benchmark), while  $\alpha = 1$  ( $\mu^+$ -benchmark) and  $\alpha = -1$  ( $\mu^-$ -benchmark) correspond to two standard deviations above and below the mean, respectively. Model calibration and fitted parameters are provided in Table 1 and follow the procedure described in Section 3.1.

## ZERO EMISSIONS: COMMITMENT MODEL INTERCOMPARISON PROJECT (ZECMIP)

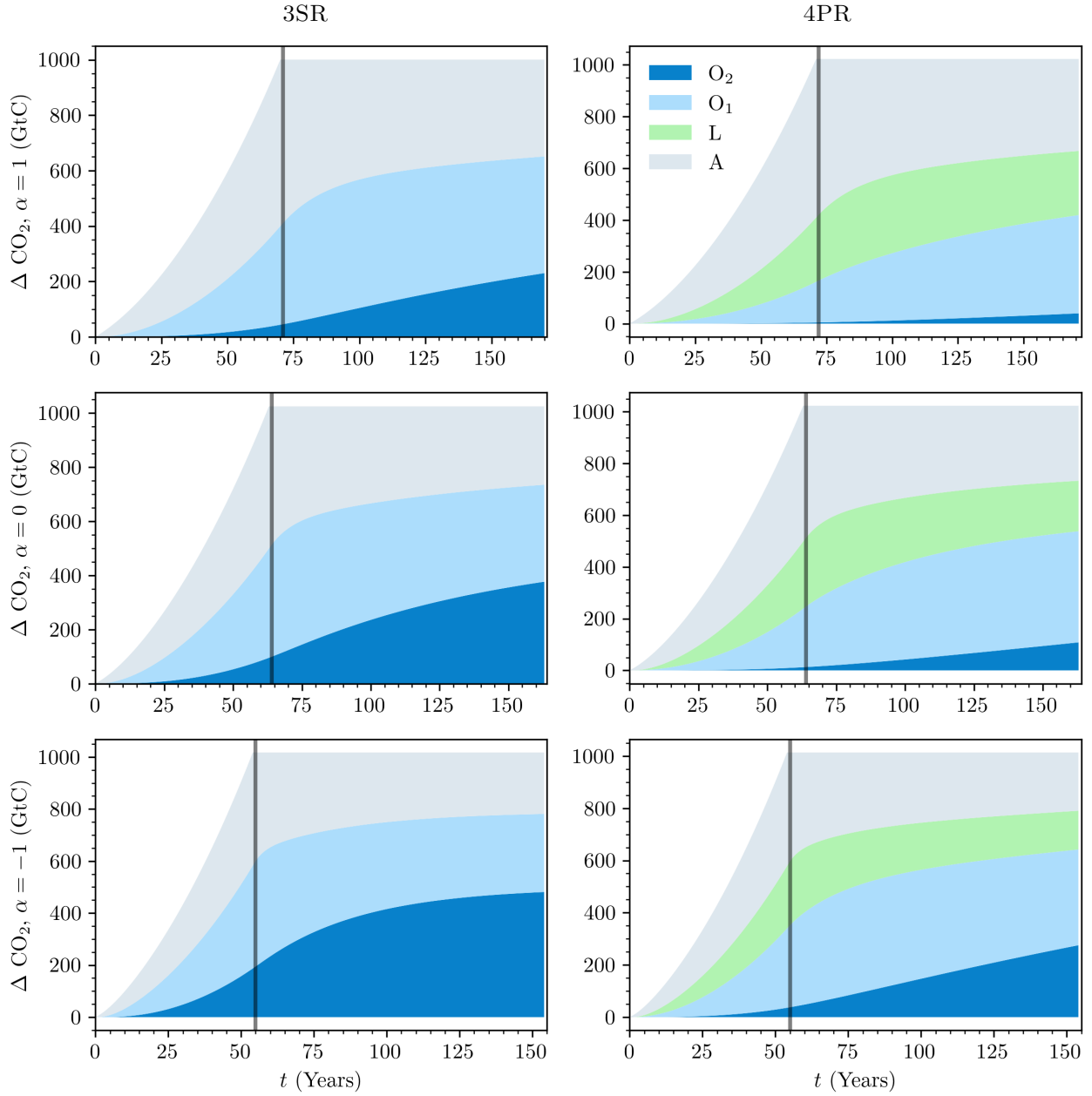
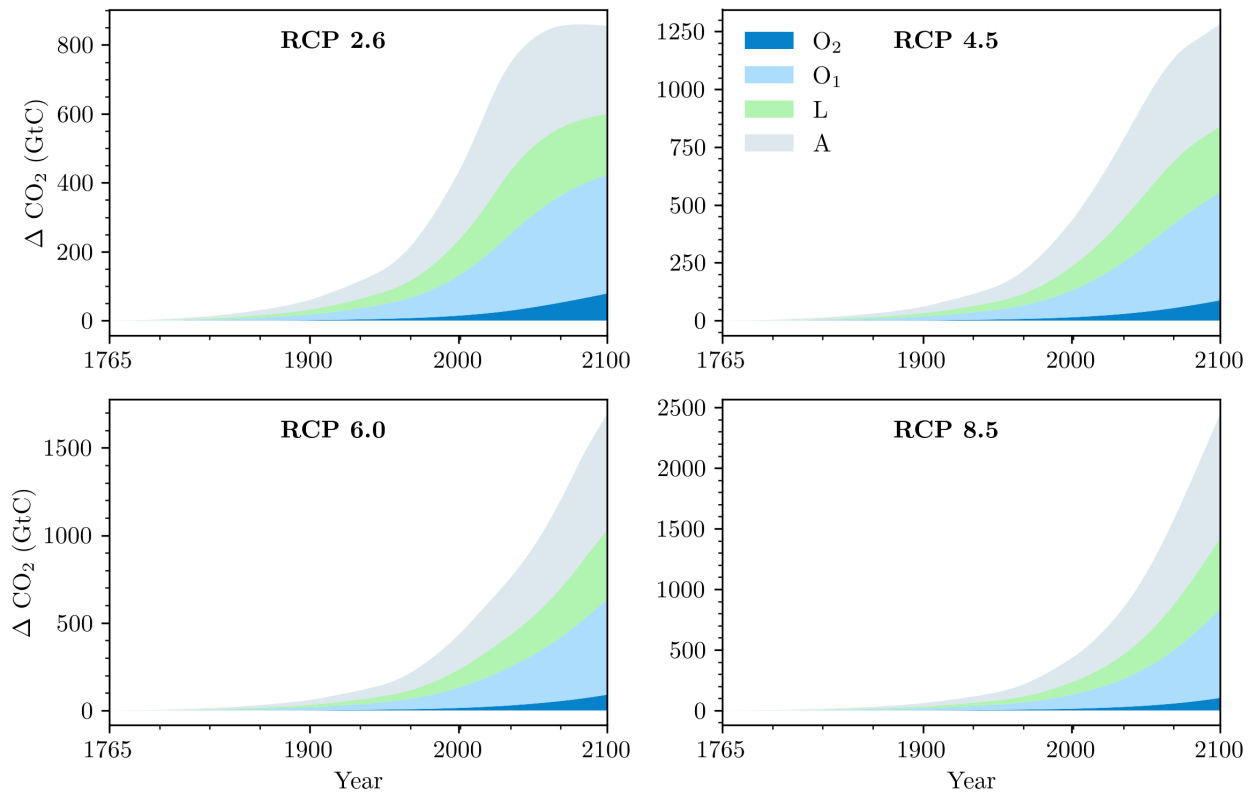


**Figure B.3:** The figure displays the change in CO<sub>2</sub> across various reservoirs relative to the pre-industrial (PI) equilibrium condition, using the weighted operator  $\mathbf{A}^\alpha$  in the 3SR (left column) and 4PR (right column) model configurations. The simulations are based on the experimental setup described in Section 4.1.2. Model calibration and fitted parameters are detailed in Table 1, following the procedure outlined in Section 3.1.

## RCP: RESERVOIR ABSORPTION (CONSTANT OPERATOR)



## RCP: RESERVOIR ABSORPTION (TIME-DEPENDANT OPERATOR)

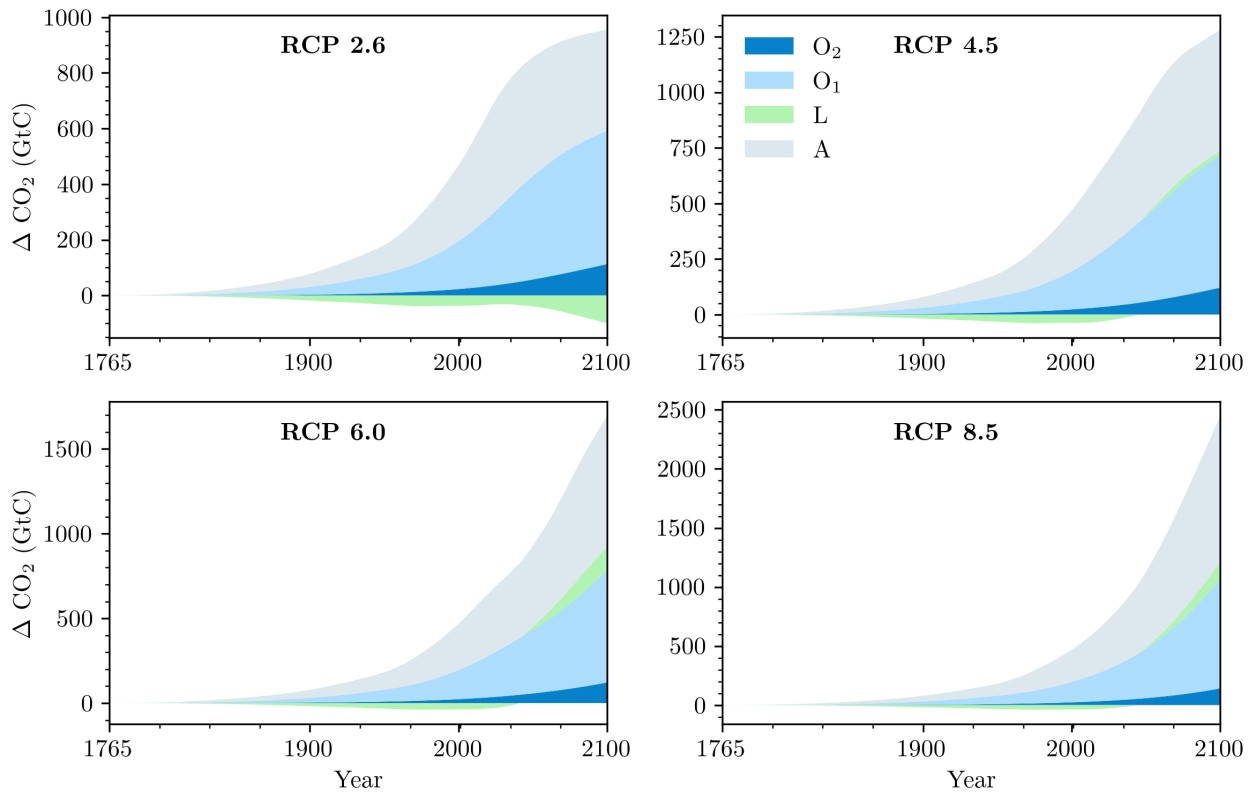


**Figure B.4:** The figure illustrates changes in CO<sub>2</sub> levels across various reservoirs relative to pre-industrial (PI) equilibrium conditions, using the 4PR model configuration for both constant (top) and time-dependent (bottom) operator simulations. The simulations are based on the experimental setup described in Section 4. Results are shown for  $\alpha = 0$ .

## C Present-Day Carbon Cycle Parameters and Simulations

### C.1 Climate Emulator Calibration and Simulations

In this Appendix, we present the same results as shown previously, recalibrated using the present-day (PD) datasets from [Joos et al. \(2013\)](#).

### C.2 Economic Results

In this Appendix, we examine the economic implications of the present-day simulations and compare them with those of the pre-industrial simulations.

Figure [C.3](#) displays the dynamics of atmospheric carbon mass (Figure [C.3a](#)) and atmospheric temperature (Figure [C.3b](#)), while Figure [C.4](#) shows the mitigation rate (Figure [C.4a](#)) and the social cost of carbon (SCC) (Figure [C.4b](#)) for both present-day (dashed lines) and pre-industrial (solid lines) simulations, comparing the 3SR and 4PR models.

In the present-day initialization, no significant differences are observed between the 3SR and 4PR models. However, present-day conditions lead to a higher accumulation of atmospheric carbon and consequently a higher atmospheric temperature.

This more pronounced climate response to the emissions results in the need for higher mitigation efforts and the increased SCC.

FITTED PARAMETERS VALUES - PRESENT DAY											
	$a_{A \rightarrow O_1}^\mu$	$a_{O_1 \rightarrow O_2}^\mu$	$a_{A \rightarrow L}^\mu$	$\tilde{m}_A^\mu$	$\tilde{m}_{O_1}^\mu$	$\tilde{m}_{O_2}^\mu$	$\tilde{m}_L^\mu$	$c^{\mu^+}$	$c^{\mu^-}$	$m_{O^e}^{t_e}/m_{L^e}^{t_e}$	$\tau$
<i>Lower</i>	$10^{-6}$	$10^{-6}$	$10^{-6}$	589	$10^{-6}$	$10^{-6}$	$10^{-6}$	$10^{-6}$	1		
<b>3SR</b>	0.0530	0.0141	-	589	433	781	-	0.3390	3.3213	-	7/78
<b>4PR</b>	0.0127	0.0015	0.0441	589	769	37,185	242	0.3364	3.7009	0.6609	6/53/1416
<i>Upper</i>	0.3	0.3	0.3	589	1,800	74,200	1,100	1	5		

**Table 6:** Similar to Table 1, but with model fitting performed using the present-day (PD) datasets from Joos et al. (2013) instead of pre-industrial (PI) data.

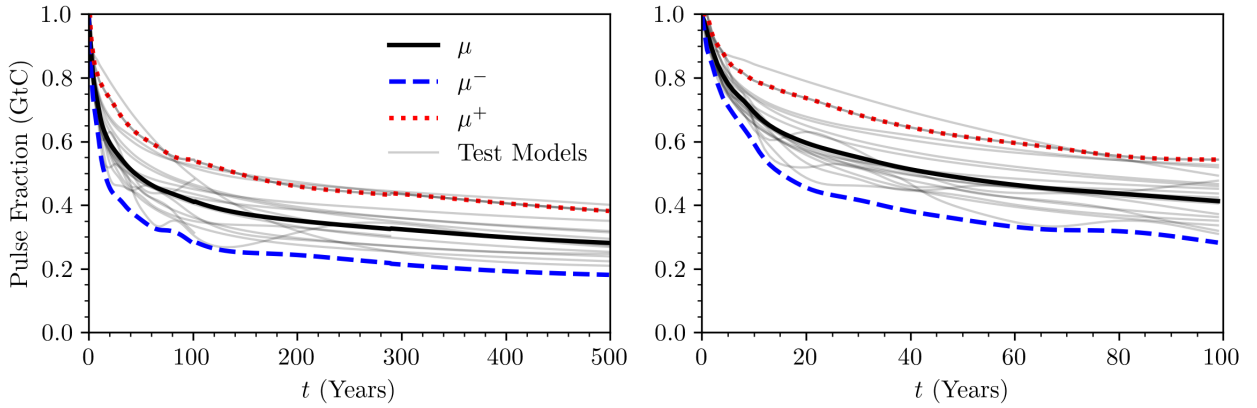


**Figure C.1:** Simulation results from Joos et al. (2013) illustrating the decay of a 100 GtC carbon pulse over the first 500 years, based on model parameters fitted to present-day (PD) settings. This figure mirrors the description of Figure 2, but uses PD benchmarks in place of pre-industrial (PI) datasets.

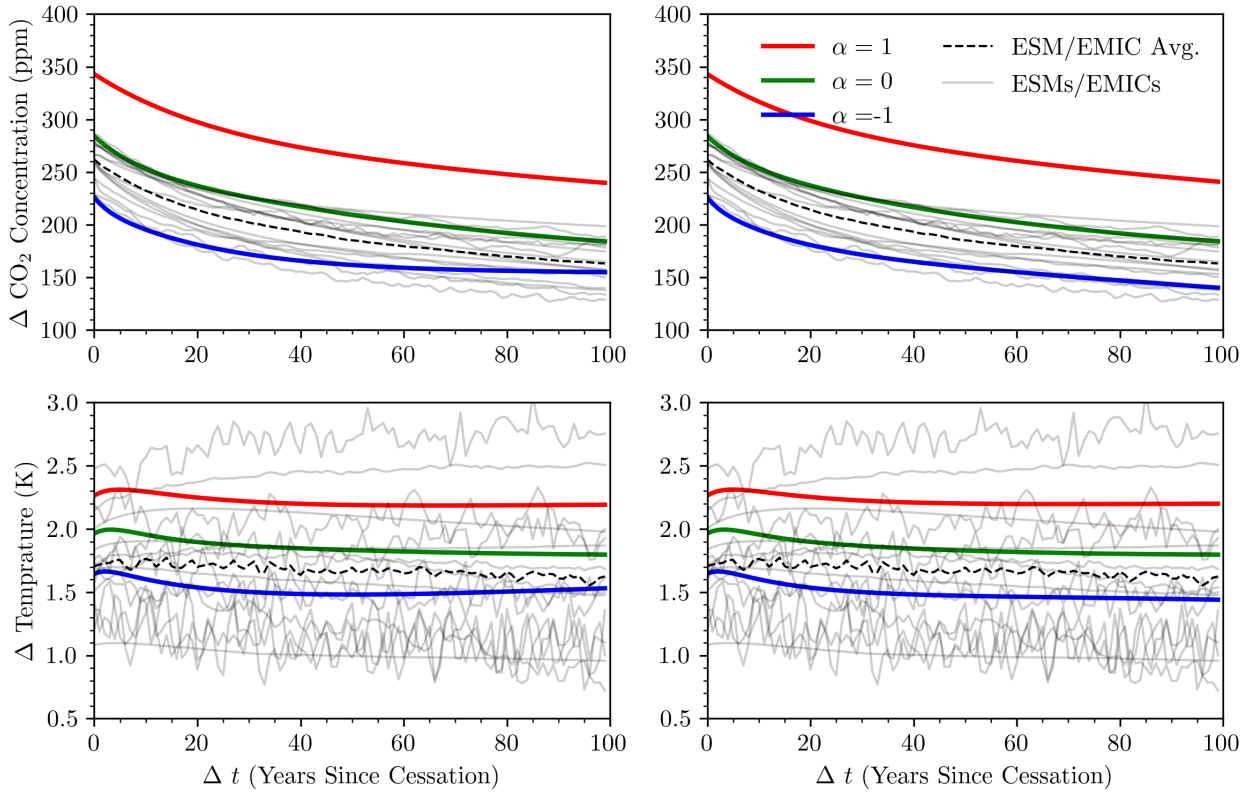
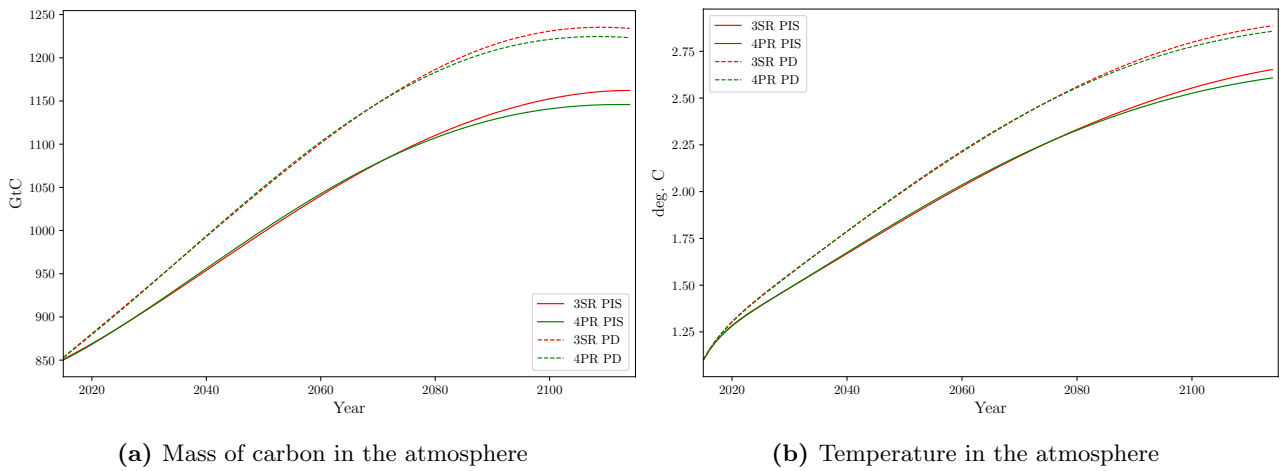


**Figure C.2:** The simulated changes in atmospheric  $\text{CO}_2$  concentrations and temperatures following the cessation event are shown for the 3SR (left column) and 4PR (right column) model configurations, with parameters fitted to present-day (PD) settings. This figure follows the description of Figure 6, but uses the PD benchmark in place of the pre-industrial (PI) datasets.



(a) Mass of carbon in the atmosphere

(b) Temperature in the atmosphere

**Figure C.3:** Optimal concentrations in the atmosphere (left panel) as well as the atmospheric temperature (right panel) for the present-day simulations.

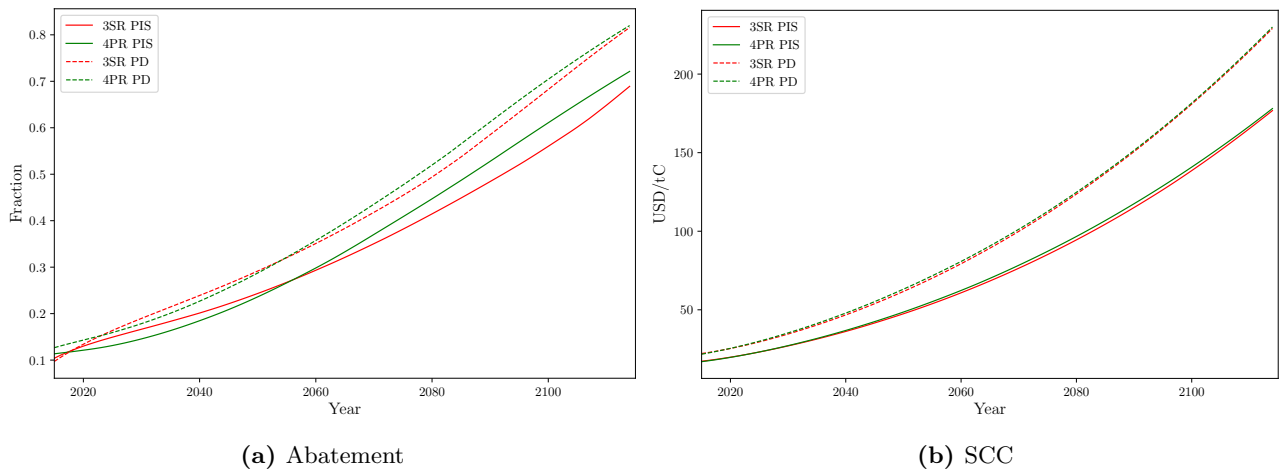


**Figure C.4:** Optimal abatement (left panel) and the social cost of carbon (SCC) (right panel) for present-day simulations.

## D More details on the IAM

This Appendix provides additional details on the IAM used in the numerical experiments in Section 5. Further details on the parametrization of exogenous variables (such as labor, total factor productivity (TFP), emission intensity), and economic parameters are available in the online Appendix of [Folini et al. \(2024\)](#).

### Parametrization of climate equations

For the temperature equations, we refer the reader to [Folini et al. \(2024\)](#). The initial values for each carbon cycle model are summarized in the table below:

Model	$\tilde{\mathbf{m}}^\mu = (\tilde{\mathbf{m}}_A^\mu, \tilde{\mathbf{m}}_{O_1}^\mu, \tilde{\mathbf{m}}_{O_2}^\mu, \tilde{\mathbf{m}}_L^\mu)$	$\mathbf{m}_{\text{ini}}^\mu = (\mathbf{m}_A^\mu, \mathbf{m}_{O_1}^\mu, \mathbf{m}_{O_2}^\mu, \mathbf{m}_L^\mu)$
3SR	(589, 752, 1289, -)	(850, 983, 1377, -)
4PR	(589, 1078, 37220, 387)	(850, 1237, 37236, 531)
4PR-X	(589, 1078, 37220, 258)	(850, 1236, 37235, 371)

**Table 7:** Labelling of the models and their respective parameterization and initial values.

It is essential to clarify the calculation of initial values. We began with the equilibrium carbon masses, representative of the 1750 carbon cycle, and then integrated the climate emulator forward using historical carbon emissions from fossil fuel use and land use changes. Integration stopped once atmospheric carbon concentrations aligned with present-day observed values, for example, 380 ppm CO<sub>2</sub> in 2005 or 401 ppm CO<sub>2</sub> in 2015.

For the dynamic 4PR-X model, the equilibrium carbon mass in the land biosphere was also updated over time. This model assumes that any land-use change emissions, such as deforestation, correspondingly reduce the equilibrium mass (storage capacity) of the land biosphere reservoir. For example, a 1 GtC emission from land use in a specific year (see Figure 4) reduces the land biosphere equilibrium mass  $\tilde{\mathbf{m}}_L^\mu$  by 1 GtC. As this reservoir's uptake capacity declines over time, the carbon accumulation in other reservoirs increases. Consequently, the 4PR-X model reaches present-day atmospheric carbon concentrations more quickly than the static models. To ensure coherence and comparability, we initialize all models at the same present-day atmospheric carbon concentrations.

## E Sensitivity Analysis

In this Appendix, we consider two cases of sensitivity analysis that are typical of IAMs. As in the main text, we provide the results for the preindustrial simulations. First, we consider the case of higher possible damages that are present due to warming. We want to learn if a possible increase in damages can elicit a different behavior from the carbon cycles under consideration. Second, we consider a sensitivity to the discount rate. We are doing so by simultaneously varying the intertemporal elasticity of substitution and pure rate of time preferences while keeping the average interest rates fixed. For more details on this approach, see [Folini et al. \(2024\)](#). For the sensitivity analysis, we consider the same three versions of carbon cycles, the three-reservoir model 3SR, the four-reservoir model 4PR, and the dynamic four-reservoir model 4PR-X.

### Sensitivity to Damages

For the increased damages scenario, we assume damages to be three times higher than in the benchmark cases. The simulation results for this scenario are shown in Figure E.5 and Figure E.6.

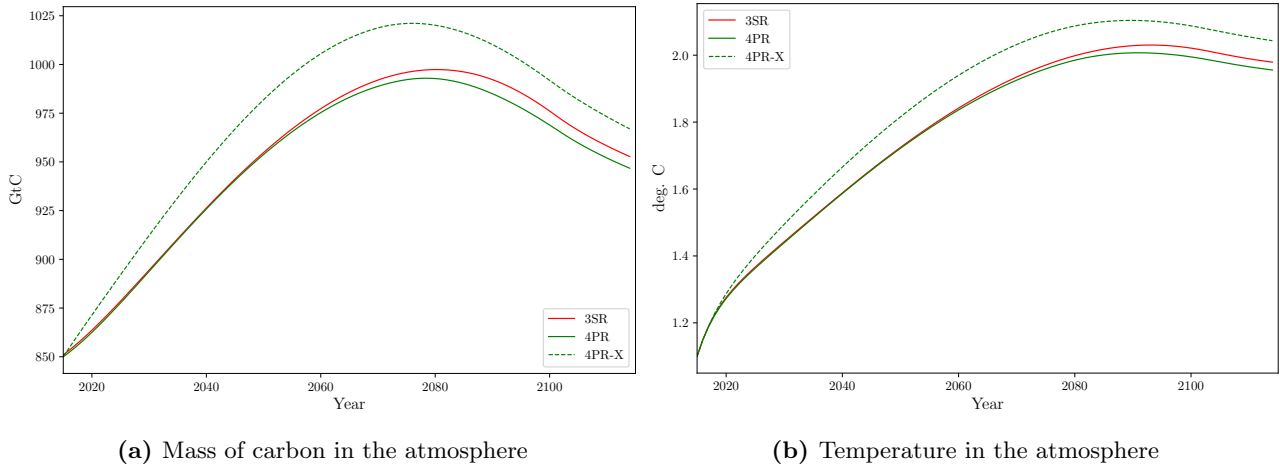


**Figure E.5:** Optimal atmospheric CO<sub>2</sub> concentrations (left panel) and atmospheric temperature (right panel) in the higher damages scenario.

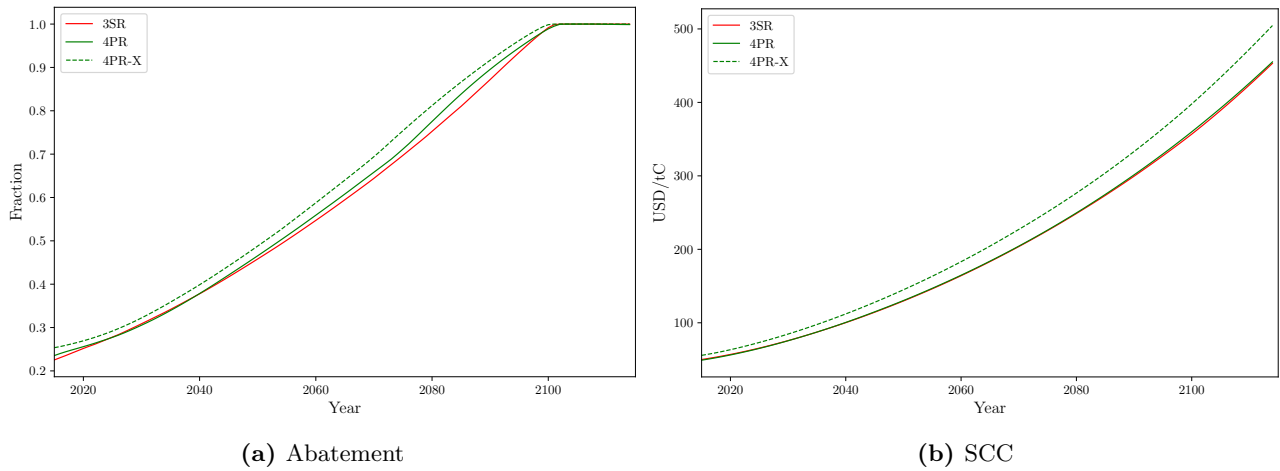


**Figure E.6:** Optimal abatement levels (left panel) and Social Cost of Carbon (SCC) (right panel) in the higher damages scenario.

In comparison to the benchmark optimal case (see Figure 10), the anticipation of higher damages drives significantly stronger mitigation efforts across all scenarios, achieving full mitigation within 80 years, whereas in the standard damage scenario, full mitigation is only reached after 100 years. This intensified mitigation results in lower atmospheric carbon concentrations and temperatures. However, the behavior of the different carbon cycles under higher damages mirrors their performance in the benchmark optimal case.

## Sensitivity to the Discount Rate

Next, we examine the sensitivity of the model's behavior under varying discount rates for different carbon cycle configurations. The results of these simulations are shown in Figures E.7 and E.8. While the carbon mass and temperature trajectories display minor differences across models with different discount rates, the SCC values remain consistent. The differences between the 3SR and 4PR models are minimal, whereas the SCC values for the 4PR-X model are consistently higher than those of the other models, as observed in the benchmark case (marked with  $\psi = 0.69$  in the graphs).

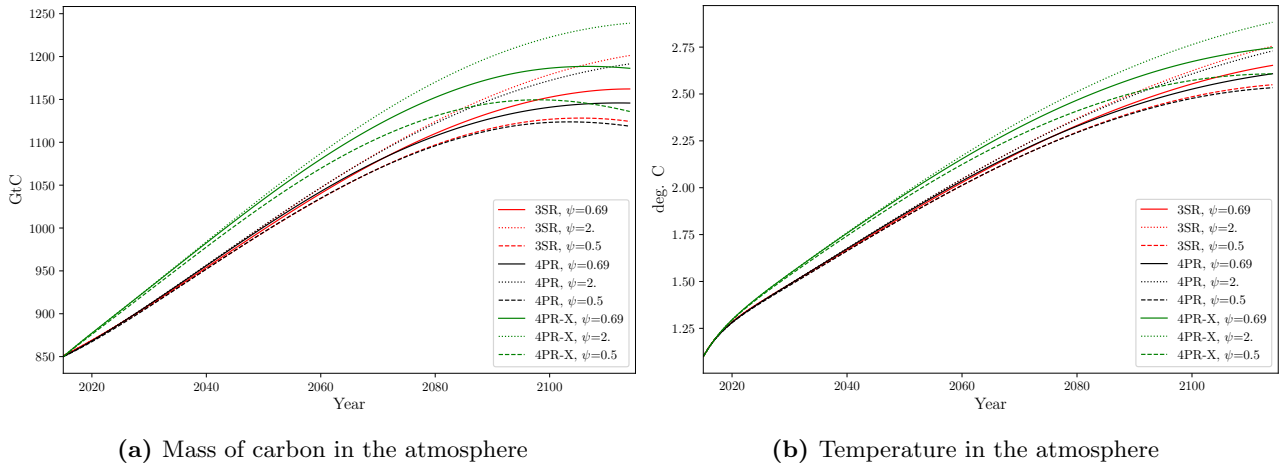


**Figure E.7:** Optimal atmospheric carbon concentrations (left panel) and atmospheric temperature (right panel) for varying discount rate values.

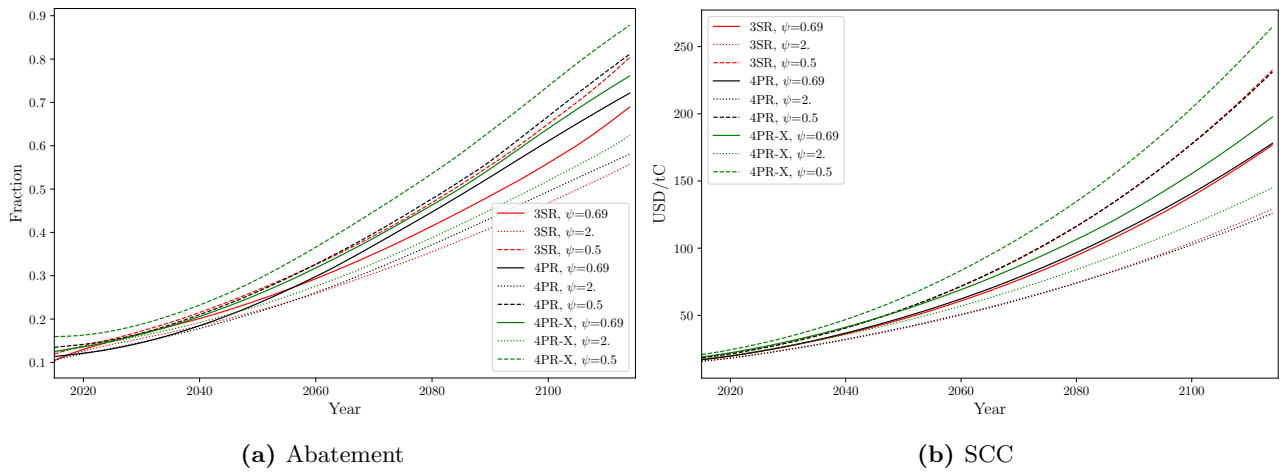


**Figure E.8:** Optimal abatement levels (left panel) and Social Cost of Carbon (SCC) values (right panel) across different discount rates.

## Bibliographies

- Arora, Vivek K., Anna Katavouta, Richard G. Williams, Chris D. Jones, Victor Brovkin, Pierre Friedlingstein, Jörg Schwinger, Laurent Bopp, Olivier Boucher, Patricia Cadule, Matthew A. Chamberlain, James R. Christian, Christine Delire, Rosie A. Fisher, Tomohiro Hajima, Tatiana Ilyina, Emilie Joetzjer, Michio Kawamiya, Charles D. Koven, John P. Krasting, Rachel M. Law, David M. Lawrence, Andrew Lenton, Keith Lindsay, Julia Pongratz, Thomas Raddatz, Roland Séférian, Kaoru Tachiiri, Jerry F. Tjiputra, Andy Wiltshire, Tongwen Wu, and Tilo Ziehn. 2020. “Carbon-concentration and carbon-climate feedbacks in CMIP6 models and their comparison to CMIP5 models.” *Biogeosciences* 17 (16):4173–4222.
- Azinovic, Marlon, Luca Gaegauf, and Simon Scheidegger. 2022. “Deep equilibrium nets.” *International Economic Review* 63 (4):1471–1525.
- Benítez, Pablo C., Pablo C. Benítez, Ian McCallum, Ian McCallum, Michael Obersteiner, Michael Obersteiner, Yoshiki Yamagata, and Yoshiki Yamagata. 2007. “Global potential for carbon sequestration: Geographical distribution, country risk and policy implications.” *Ecological Economics* .
- Beusch, Lea, Lukas Gudmundsson, and Sonia I. Seneviratne. 2020. “Emulating Earth system model temperatures with MESMER: from global mean temperature trajectories to grid-point-level realizations on land.” *Earth System Dynamics* 11 (1):139–159.
- Bossy, Thomas, Thomas Gasser, and Philippe Ciais. 2022. “Pathfinder v1.0.1: a Bayesian-inferred simple carbon-climate model to explore climate change scenarios.” *Geoscientific Model Development* 15 (23):8831–8868.
- Cai, Yongyang and Thomas Lontzek. 2019. “The social cost of carbon with economic and climate risks.” *Journal of Political Economy* 127 (6):2684–2734.
- Calvin, Katherine, Katherine Calvin, Marshall Wise, Marshall Wise, Page Kyle, Page Kyle, G. Page Kyle, Pralit Patel, Pralit Patel, Leon Clarke, Leon E. Clarke, James A. Edmonds, and James A. Edmonds. 2014. “Trade-offs of different land and bioenergy policies on the path to achieving climate targets.” *Climatic Change* .
- Ciais, P., C. Sabine, G. Bala, L. Bopp, V. Brovkin, et al., and Joanna Isobel House. 2014. *Carbon and Other Biogeochemical Cycles*. United Kingdom: Cambridge University Press, 465–570.
- Dietz, Simon, Frederick Van Der Ploeg, Armon Rezai, and Frank Venmans. 2020. “Department of Economics Discussion Paper Series Are economists getting climate dynamics right and does it matter? Are economists getting climate dynamics right and does it matter?” (900).
- Dietz, Simon and Frank Venmans. 2019. “Cumulative carbon emissions and economic policy: In search of general principles.” *Journal of Environmental Economics and Management* 96:108–129. URL <https://doi.org/10.1016/j.jeem.2019.04.003>.
- Doelman, Jonathan C., Jonathan C. Doelman, Jonathan Doelman, Jonathan C. Doelman, Jonathan C. Doelman, Elke Stehfest, Elke Stehfest, Elke Stehfest, Detlef P. van Vuuren, Detlef P. van Vuuren, Andrzej Tabeau, Andrzej Tabeau, Andries F. Hof, Andries F. Hof, Maarten C. Braakhekke, Maarten C. Braakhekke, David Gernaat, David E.H.J. Gernaat, Maarten van den Berg, Maarten van den Berg, Willem Jan van Zeist, Willem-Jan van Zeist, Willem Jan van Zeist, Willem-Jan van Zeist, Willem Jan van Zeist, Vassilis Daioglou, Vassilis Daioglou, Hans van Meijl, Hans van Meijl, Hans van Meijl, Paul L. Lucas, and Paul L. Lucas. 2020. “Afforestation for climate change mitigation: Potentials, risks and trade-offs.” *Global Change Biology* .

- Dorheim, Kalyn, Skylar Gering, Robert Gieseke, Corinne Hartin, Leeya Pressburger, Alexey N. Shiklomanov, Steven J. Smith, Claudia Tebaldi, Dawn L. Woodard, and Ben Bond-Lamberty. 2024. “Hector V3.2.0: Functionality And Performance Of A Reduced-Complexity Climate Model.” *Geoscientific Model Development* 17:4855–4869.
- Dorheim, Kalyn, Steven J. Smith, and Ben Bond-Lamberty. 2021. “HIRM v1.0: a hybrid impulse response model for climate modeling and uncertainty analyses.” *Geoscientific Model Development* 14 (1):365–375.
- Fernández-Villaverde, Jesús, Kenneth Gillingham, and Simon Scheidegger. 2024. “Climate Change through the Lens of Macroeconomic Modeling.” Working Paper 32963, National Bureau of Economic Research. URL <http://www.nber.org/papers/w32963>.
- Folini, Doris, Aleksandra Friedl, Felix Kübler, and Simon Scheidegger. 2024. “The climate in climate economics.” *Review of Economic Studies* :rdae011.
- Friedl, Aleksandra, Felix Kübler, Simon Scheidegger, and Takafumi Usui. 2023. “Deep uncertainty quantification: With an application to integrated assessment models.” Working paper, University of Lausanne.
- Fuss, Sabine, William F. Lamb, Max W. Callaghan, Jérôme Hilaire, Felix Creutzig, Thorben Amann, Tim Beringer, Wagner de Oliveira Garcia, Jens Hartmann, Tarun Khanna, Gunnar Luderer, Gregory F. Nemet, Joeri Rogelj, Pete Smith, José Luis Vicente Vicente, Jennifer Wilcox, Maria del Mar Zamora Dominguez, and Jan C. Minx. 2018. “Negative emissions—Part 2: Costs, potentials and side effects.” *Environmental Research Letters* 13 (6):063002.
- Gasser, Thomas, Philippe Ciais, Olivier Boucher, Yann Quilcaille, Maxime Tortora, Laurent Bopp, and Didier Hauglustaine. 2017. “The compact Earth system model OSCAR v2.2: description and first results.” *Geoscientific Model Development* 10 (1):271–319.
- Geoffroy, Olivier, D. Saint-Martin, G. Bellon, A. Voldoire, D. J.L. Olivié, and S. Tytéca. 2013a. “Transient climate response in a two-layer energy-balance model. Part II: Representation of the efficacy of deep-ocean heat uptake and validation for CMIP5 AOGCMs.” *Journal of Climate* 26 (6):1859–1876.
- Geoffroy, Olivier, D. Saint-martin, D. J.L. Olivié, A. Voldoire, G. Bellon, and S. Tytéca. 2013b. “Transient climate response in a two-layer energy-balance model. Part I: Analytical solution and parameter calibration using CMIP5 AOGCM experiments.” *Journal of Climate* 26 (6):1841–1857.
- Hassler, John, Per Krusell, and Conny Olovsson. 2024. “Sustainability.” In *Macroeconomics*, chap. 23. <https://phdmacrobook.org/>.
- Hertel, Thomas W., Thomas W. Hertel, Huey-Lin Lee, Huey-Lin Lee, Steven K. Rose, Steven K. Rose, Steven K. Rose, Brent Sohngen, and Brent Sohngen. 2008. “Modeling Land-use Related Greenhouse Gas Sources and Sinks and their Mitigation Potential.” *GTAP Working Paper* .
- Hooss, G., R. Voss, K. Hasselmann, E. Maier-Reimer, and F. Joos. 2001. “A nonlinear impulse response model of the coupled carbon cycle-climate system (NICCS).” *Climate Dynamics* 18 (3-4):189–202.
- Houghton, John Theodore, G. J. Jenkins, and J. J. Ephraums, editors. 1990. *Climate Change: The IPCC Scientific Assessment*. Cambridge University Press. URL <https://www.cambridge.org/eng/academic/subjects/earth-and-environmental-science/climatology-and-climate-change/climate-change-ipcc-scientific-assessment>. 410 pp., Hardback.
- Hurt, G. C., L. P. Chini, S. Frohling, R. A. Betts, J. Feddema, G. Fischer, J. P. Fisk, K. Hibbard, R. A. Houghton, A. Janetos, C. D. Jones, G. Kindermann, T. Kinoshita, Kees Klein Goldewijk,

- K. Riahi, E. Shevliakova, S. Smith, E. Stehfest, A. Thomson, P. Thornton, D. P. van Vuuren, and Y. P. Wang. 2011. “Harmonization of land-use scenarios for the period 1500–2100: 600 years of global gridded annual land-use transitions, wood harvest, and resulting secondary lands.” *Climatic Change* 109 (1):117. URL <https://doi.org/10.1007/s10584-011-0153-2>.
- Joos, Fortunat, Raphael Roth, Jan S Fuglestedt, Glen P Peters, Ian G Enting, W von Bloh, Victor Brovkin, Eleanor J Burke, Michael Eby, Neil R Edwards et al. 2013. “Carbon dioxide and climate impulse response functions for the computation of greenhouse gas metrics: a multi-model analysis.” *Atmospheric Chemistry and Physics* 13 (5):2793–2825.
- Krey, Volker, Gunnar Luderer, Leon Clarke, and Elmar Kriegler. 2014. “Getting from here to there - energy technology transformation pathways in the EMF27 scenarios.” *Climatic Change* 123 (3-4):369–382.
- Leach, Nicholas J., Stuart Jenkins, Zebedee Nicholls, Christopher J. Smith, John Lynch, Michelle Cain, Tristram Walsh, Bill Wu, Junichi Tsutsui, and Myles R. Allen. 2021. “FaIRv2.0.0: a generalized impulse response model for climate uncertainty and future scenario exploration.” *Geoscientific Model Development* 14 (5):3007–3036.
- Li, Sile, Andrew J. Jarvis, and David T. Leedal. 2009. “Are response function representations of the global carbon cycle ever interpretable?” *Tellus Series B Chemical and Physical Meteorology B* 61 (2):361–371.
- MacDougall, A. H., T. L. Frölicher, C. D. Jones, J. Rogelj, H. D. Matthews, K. Zickfeld, V. K. Arora, N. J. Barrett, V. Brovkin, F. A. Burger, M. Eby, A. V. Eliseev, T. Hajima, P. B. Holden, A. Jeltsch-Thömmes, C. Koven, N. Mengis, L. Menviel, M. Michou, I. I. Mokhov, A. Oka, J. Schwinger, R. Séférian, G. Shaffer, A. Sokolov, K. Tachiiri, J. Tjiputra, A. Wiltshire, and T. Ziehn. 2020. “Is there warming in the pipeline? A multi-model analysis of the Zero Emissions Commitment from CO<sub>2</sub>.” *Biogeosciences* 17 (11):2987–3016. URL <https://bg.copernicus.org/articles/17/2987/2020/>.
- MacDougall, Andrew H. 2016. “The Transient Response to Cumulative CO<sub>2</sub> Emissions: a Review.” *Current Climate Change Reports* 2 (1):39–47.
- Meinshausen, Malte, S. J. Smith, K. Calvin, J. S. Daniel, M. L. T. Kainuma, J. F. Lamarque, K. Matsumoto, S. A. Montzka, S. C. B. Raper, K. Riahi, A. Thomson, G. J. M. Velders, and D. P. P. van Vuuren. 2011. “The RCP greenhouse gas concentrations and their extensions from 1765 to 2300.” *Climatic Change* 109 (1-2):213–241.
- Melnikova, Irina, Philippe Ciais, Olivier Boucher, and Katsumasa Tanaka. 2023. “Assessing carbon cycle projections from complex and simple models under SSP scenarios.” *Climatic Change* 176 (12):168.
- Millar, Richard J, Zebedee R Nicholls, Pierre Friedlingstein, and Myles R Allen. 2017. “A modified impulse-response representation of the global near-surface air temperature and atmospheric concentration response to carbon dioxide emissions.” *Atmospheric Chemistry and Physics* 17 (11):7213–7228.
- Minx, Jan C., William F. Lamb, Max W. Callaghan, Sabine Fuss, Jérôme Hilaire, Felix Creutzig, Thorben Amann, Tim Beringer, Wagner de Oliveira Garcia, Jens Hartmann, Tarun Khanna, Dominic Lenzi, Gunnar Luderer, Gregory F. Nemet, Joeri Rogelj, Pete Smith, Jose Luis Vicente Vicente, Jennifer Wilcox, and Maria del Mar Zamora Dominguez. 2018. “Negative emissions: Part 1—research landscape and synthesis.” *Environmental Research Letters* 13 (6):063001.

Mo, Lidong, Constantin M. Zohner, Peter B. Reich, Jingjing Liang, Sergio de Miguel, Gert-Jan Nabuurs, Susanne S. Renner, Johan van den Hoogen, Arnan Araza, Martin Herold, Leila Mirzaghali, Haozhi Ma, Colin Averill, Oliver L. Phillips, Javier G. P. Gamarra, Iris Hordijk, Devin Routh, Meinrad Abegg, Yves C. Adou Yao, Giorgio Alberti, Angelica M. Almeyda Zambrano, Braulio Vilchez Alvarado, Esteban Alvarez-Dávila, Patricia Alvarez-Loayza, Luciana F. Alves, Iêda Amaral, Christian Ammer, Clara Antón-Fernández, Alejandro Araujo-Murakami, Luzmila Arroyo, Valerio Avitabile, Gerardo A. Aymard, Timothy R. Baker, Radomir Bałazy, Olaf Banki, Jorcely G. Barroso, Meredith L. Bastian, Jean-Francois Bastin, Luca Birigazzi, Philippe Birnbaum, Robert Bitariho, Pascal Boeckx, Frans Bongers, Olivier Bouriaud, Pedro H. S. Brancalion, Susanne Brandl, Francis Q. Brearley, Roel Brienen, Eben N. Broadbent, Helge Bruelheide, Filippo Bussotti, Roberto Cazzolla Gatti, Ricardo G. César, Goran Cesljar, Robin L. Chazdon, Han Y. H. Chen, Chelsea Chisholm, Hyunkook Cho, Emil Cienciala, Connie Clark, David Clark, Gabriel D. Colletta, David A. Coomes, Fernando Cornejo Valverde, José J. Corral-Rivas, Philip M. Crim, Jonathan R. Cumming, Selvadurai Dayanandan, André L. de Gasper, Mathieu Decuyper, Géraldine Derroire, Ben DeVries, Ilija Djordjevic, Jiri Dolezal, Aurélie Dourdain, Nestor Laurier Engone Obiang, Brian J. Enquist, Teresa J. Eyre, Adandé Belarmain Fandohan, Tom M. Fayle, Ted R. Feldpausch, Leandro V. Ferreira, Leena Finér, Markus Fischer, Christine Fletcher, Lorenzo Frizzera, Damiano Gianelle, Henry B. Glick, David J. Harris, Andrew Hector, Andreas Hemp, Geerten Hengeveld, Bruno Hérault, John L. Herbohn, Annika Hillers, Eurídice N. Honorio Coronado, Cang Hui, Thomas Ibanez, Nobuo Imai, Andrzej M. Jagodziński, Bogdan Jaroszewicz, Vivian Kvist Johannsen, Carlos A. Joly, Tommaso Jucker, Ilbin Jung, Viktor Karminov, Kuswata Kartawinata, Elizabeth Kearsley, David Kenfack, Deborah K. Kennard, Sebastian Kepfer-Rojas, Gunnar Keppel, Mohammed Latif Khan, Timothy J. Killeen, Hyun Seok Kim, Kanehiro Kitayama, Michael Köhl, Henn Korjus, Florian Kraxner, Dmitry Kucher, Diana Laarmann, Mait Lang, Huicui Lu, Natalia V. Lukina, Brian S. Maitner, Yadvinder Malhi, Eric Marcon, Beatriz Schwantes Marimon, Ben Hur Marimon-Junior, Andrew R. Marshall, Emanuel H. Martin, Jorge A. Meave, Omar Melo-Cruz, Casimiro Mendoza, Irina Mendoza-Polo, Stanislaw Miscicki, Cory Merow, Abel Monteagudo Mendoza, Vanessa S. Moreno, Sharif A. Mukul, Philip Mundhenk, María Guadalupe Nava-Miranda, David Neill, Victor J. Neldner, Radovan V. Nevenic, Michael R. Ngugi, Pascal A. Niklaus, Jacek Oleksyn, Petr Ontikov, Edgar Ortiz-Malavasi, Yude Pan, Alain Paquette, Alexander Parada-Gutierrez, Elena I. Parfenova, Minjee Park, Marc Parren, Narayanaswamy Parthasarathy, Pablo L. Peri, Sebastian Pfautsch, Nicolas Picard, Maria Teresa F. Piedade, Daniel Piotta, Nigel C. A. Pitman, Axel Dalberg Poulsen, John R. Poulsen, Hans Pretzsch, Freddy Ramirez Arevalo, Zorayda Restrepo-Correa, Mirco Rodeghiero, Samir G. Rolim, Anand Roopsind, Francesco Rovero, Ervan Rutishauser, Purabi Saikia, Christian Salas-Eljatib, Philippe Saner, Peter Schall, Mart-Jan Schelhaas, Dmitry Schepaschenko, Michael Scherer-Lorenzen, Bernhard Schmid, Jochen Schöngart, Eric B. Searle, Vladimír Seben, Josep M. Serra-Diaz, Douglas Sheil, Anatoly Z. Shvidenko, Javier E. Silva-Espejo, Marcos Silveira, James Singh, Plinio Sist, Ferry Slik, Bonaventure Sonké, Alexandre F. Souza, Krzysztof J. Stereńczak, Jens-Christian Svenning, Miroslav Svoboda, Ben Swanepoel, Natalia Targhetta, Nadja Tchebakova, Hans ter Steege, Raquel Thomas, Elena Tikhonova, Peter M. Umunay, Vladimir A. Usoltsev, Renato Valencia, Fernando Valladares, Fons van der Plas, Tran Van Do, Michael E. van Nuland, Rodolfo M. Vasquez, Hans Verbeeck, Helder Viana, Alexander C. Vibrans, Simone Vieira, Klaus von Gadow, Hua-Feng Wang, James V. Watson, Gijsbert D. A. Werner, Susan K. Wiser, Florian Wittmann, Hannsjoerg Woell, Verginia Wortel, Roderik Zagt, Tomasz Zawila-Niedzwiecki, Chunyu Zhang, Xiuhai Zhao, Mo Zhou, Zhi-Xin Zhu, Irie C. Zo-Bi, George D. Gann, and Thomas W. Crowther. 2023. “Integrated global assessment of the natural forest carbon potential.” *Nature* 624 (7990):92–101.

Nemet, Gregory F., Max W. Callaghan, Felix Creutzig, Sabine Fuss, Jens Hartmann, Jérôme Hilaire, William F. Lamb, Jan C. Minx, Sophia Rogers, and Pete Smith. 2018. “Negative emissions—Part 3: Innovation and upscaling.” *Environmental Research Letters* 13 (6):063003.

Nicholls, Z., M. Meinshausen, J. Lewis, M. Rojas Corradi, K. Dorheim, T. Gasser, R. Gieseke,

- A. P. Hope, N. J. Leach, L. A. McBride, Y. Quilcaille, J. Rogelj, R. J. Salawitch, B. H. Samset, M. Sandstad, A. Shiklomanov, R. B. Skeie, C. J. Smith, S. J. Smith, X. Su, J. Tsutsui, B. Vega-Westhoff, and D. L. Woodard. 2021. “Reduced Complexity Model Intercomparison Project Phase 2: Synthesizing Earth System Knowledge for Probabilistic Climate Projections.” *Earth’s Future* 9 (6):e2020EF001900.
- Nicholls, Z. R. J., R. Gieseke, J. Lewis, A. Nauels, and M. Meinshausen. 2020. “Implications of nonlinearities between cumulative CO<sub>2</sub> emissions and CO<sub>2</sub>-induced warming for assessing the remaining carbon budget.” *Environmental Research Letters* 15 (7):074017.
- Nordhaus, William D. 2017. “Revisiting the social cost of carbon.” *Proceedings of the National Academy of Sciences of the United States of America* 114 (7):1518–1523.
- Quilcaille, Yann, Lukas Gudmundsson, and Sonia I. Seneviratne. 2023. “Extending MESMER-X: a spatially resolved Earth system model emulator for fire weather and soil moisture.” *Earth System Dynamics* 14 (6):1333–1362.
- Raupach, M. R. 2013. “The exponential eigenmodes of the carbon-climate system, and their implications for ratios of responses to forcings.” *Earth System Dynamics* 4 (1):31–49.
- Raupach, Michael R., Josep G. Canadell, Philippe Ciais, Pierre Friedlingstein, Peter J. Rayner, and Catherine M. Trudinger. 2011. “The relationship between peak warming and cumulative CO<sub>2</sub> emissions, and its use to quantify vulnerabilities in the carbon-climate-human system.” *Tellus Series B Chemical and Physical Meteorology B* 63 (2):145–164.
- Ruehr, Sophie, Trevor F Keenan, Christopher Williams, Yu Zhou, Xinchun Lu, Ana Bastos, Josep G Canadell, Iain Colin Prentice, Stephen Sitch, and César Terrer. 2023. “Evidence and attribution of the enhanced land carbon sink.” *Nature Reviews Earth & Environment* 4 (8):518–534.
- Sandstad, Marit, Borgar Aamaas, Ane Nordlie Johansen, Marianne Tronstad Lund, Glen Philip Peters, Bjørn Hallvard Samset, Benjamin Mark Sanderson, and Ragnhild Bieltvedt Skeie. 2024. “Cicero Simple Climate Model (Cicero-Scm V1.1.1) – An Improved Simple Climate Model With A Parameter Calibration Tool.” *Geoscientific Model Development* 17:6589–6625.
- Schwarber, Adria K., Steven J. Smith, Corinne A. Hartin, Benjamin Aaron Vega-Westhoff, and Ryan Sriver. 2019. “Evaluating climate emulation: fundamental impulse testing of simple climate models.” *Earth System Dynamics* 10 (4):729–739.
- Sohngen, Brent, Robert Mendelsohn, and Roger Sedjo. 1999. “Forest management, conservation, and global timber markets.” *American Journal of Agricultural Economics* 81 (1):1–13.
- Sohngen, Brent, Brent Sohngen, Robert Mendelsohn, and Robert Mendelsohn. 2003. “An Optimal Control Model of Forest Carbon Sequestration.” *American Journal of Agricultural Economics* .
- Sohngen, Brent, Brent Sohngen, Roger Sedjo, Brent Sohngen, Roger A. Sedjo, and Roger A. Sedjo. 2006. “Carbon Sequestration in Global Forests Under Different Carbon Price Regimes.” *The Energy Journal* .
- Traeger, Christian P. 2014. “A 4-States DICE: Quantitatively Addressing Uncertainty Effects in Climate Change.” *Environmental and Resource Economics* 59 (1):1–37.
- Tsutsui, Junichi. 2022. “Minimal CMIP Emulator (MCE v1. 2): a new simplified method for probabilistic climate projections.” *Geoscientific Model Development* 15 (3):951–970.
- van Vuuren, Detlef, Detlef P. van Vuuren, Laura Batlle-Bayer, Laura Batlle Bayer, Clifford Chuwah, Clifford Chuwah, L. Ganzeveld, Laurens Ganzeveld, Wilco Hazeleger, Wilco Hazeleger, B. J. J. M.

- van den Hurk, Bart van den Hurk, Bart van den Hurk, Twan van Noije, Twan van Noije, Brian C. O'Neill, Brian C. O'Neill, Bart J. Strengers, and Bart J. Strengers. 2012. "A comprehensive view on climate change: coupling of earth system and integrated assessment models." *Environmental Research Letters* .
- von Schuckmann, Karina, Audrey Minière, Flora Gues, Francisco José Cuesta-Valero, Gottfried Kirchengast, Susheel Adusumilli, Fiammetta Straneo, Michaël Ablain, Richard P. Allan, Paul M. Barker, Hugo Beltrami, Alejandro Blazquez, Tim Boyer, Lijing Cheng, John Church, Damien Desbruyeres, Han Dolman, Catia M. Domingues, Almudena García-García, Donata Giglio, John E. Gilson, Maximilian Gorfer, Leopold Haimberger, Maria Z. Hakuba, Stefan Hendricks, Shigeki Hosoda, Gregory C. Johnson, Rachel Killick, Brian King, Nicolas Kolodziejczyk, Anton Korosov, Gerhard Krinner, Mikael Kuusela, Felix W. Landerer, Moritz Langer, Thomas Lavergne, Isobel Lawrence, Yuehua Li, John Lyman, Florence Marti, Ben Marzeion, Michael Mayer, Andrew H. MacDougall, Trevor McDougall, Didier Paolo Monselesan, Jan Nitzbon, Inès Otosaka, Jian Peng, Sarah Purkey, Dean Roemmich, Kanako Sato, Katsunari Sato, Abhishek Savita, Axel Schweiger, Andrew Shepherd, Sonia I. Seneviratne, Leon Simons, Donald A. Slater, Thomas Slater, Andrea K. Steiner, Toshio Suga, Tanguy Szekely, Wim Thiery, Mary-Louise Timmermans, Inne Vanderkelen, Susan E. Wjiffels, Tonghua Wu, and Michael Zemp. 2023. "Heat stored in the Earth system 1960-2020: where does the energy go?" *Earth System Science Data* 15 (4):1675–1709.
- Walker, Wayne S., Seth R. Gorelik, Susan C. Cook-Patton, Alessandro Baccini, Mary K. Farina, Kylene K. Solvik, Peter W. Ellis, Jon Sanderman, Richard A. Houghton, Sara M. Leavitt, Christopher R. Schwalm, and Bronson W. Griscom. 2022. "The global potential for increased storage of carbon on land." *Proceedings of the National Academy of Science* 119 (23):e2111312119.
- Watson-Parris, D., Y. Rao, D. Olivie, Ø. Seland, P. Nowack, G. Camps-Valls, P. Stier, S. Bouabid, M. Dewey, E. Fons, J. Gonzalez, P. Harder, K. Jeggle, J. Lenhardt, P. Manshausen, M. Novitasari, L. Ricard, and C. Roesch. 2022. "ClimateBench v1.0: A Benchmark for Data-Driven Climate Projections." *Journal of Advances in Modeling Earth Systems* 14 (10):e2021MS002954.
- Weyant, John P. 2017. "Some Contributions of Integrated Assessment Models of Global Climate Change." *Review of Environmental Economics and Policy* .
- Zhang, Xuanze, Ying-Ping Wang, Peter J. Rayner, Philippe Ciais, Kun Huang, Yiqi Luo, Shilong Piao, Zhonglei Wang, Jianyang Xia, Wei Zhao, Xiaogu Zheng, Jing Tian, and Yongqiang Zhang. 2021. "A small climate-amplifying effect of climate-carbon cycle feedback." *Nature Communications* 12:2952.
- Zickfeld, Kirsten, Deven Azevedo, Sabine Mathesius, and H. Damon Matthews. 2021. "Asymmetry in the climate-carbon cycle response to positive and negative CO2 emissions." *Nature Climate Change* 11 (7):613–617. URL [https://ideas.repec.org/a/nat/natcli/v11y2021i7d10.1038\\_s41558-021-01061-2.html](https://ideas.repec.org/a/nat/natcli/v11y2021i7d10.1038_s41558-021-01061-2.html).